Solids Under Extreme Shear: Friction-Mediated Subsurface Structural Transformations

Christian Greiner, Johanna Gagel, and Peter Gumbsch*

Tribological contacts consume a significant amount of the world's primary energy due to friction and wear in different products from nanoelectromechanical systems to bearings, gears, and engines. The energy is largely dissipated in the material underneath the two surfaces sliding against each other. This subsurface material is thereby exposed to extreme amounts of shear deformation and often forms layered subsurface microstructures with reduced grain size. Herein, the elementary mechanisms for the formation of subsurface microstructures are elucidated by systematic model experiments and discrete dislocation dynamics simulations in dry frictional contacts. The simulations show how pre-existing dislocations transform into prismatic dislocation structures under tribological loading. The stress field under a moving spherical contact and the crystallographic orientation are crucial for the formation of these prismatic structures. Experimentally, a localized dislocation structure at a depth of ≈100–150 nm is found already after the first loading pass. This dislocation structure is shown to be connected to the inhomogeneous stress field under the moving contact. The subsequent microstructural transformations and the mechanical properties of the surface layer are determined by this structure. These results hold promise at guiding material selection and alloy development for tribological loading, yielding materials tailored for specific tribological scenarios.

1. Introduction

Reducing global energy consumption has a direct impact on CO_2 release which is connected with global warming, declining crop production and glacier melting.[1] A key component for reducing energy consumption is a seemingly unlikely candidate: tribology. Tribology is the study of interacting surfaces in relative motion, including friction, wear and lubrication. In the transportation sector, a third of the energy consumed is lost by overcoming friction.[2] As far back as 1977, it was estimated that 11% of the energy used by the transportation, the industrial and the utilities sectors could be saved by new developments in tribology.[3]

Although the term "tribology" was only coined in the 1960s,[4] tribological technologies date back to antiquity. Starting a fire by rubbing two pieces of wood together was only possible due to frictional heating. Transportation of the massive stone building blocks of the pyramids required lubricated contacts.[5] Since ancient times, scientific interest in friction and wear has come in cycles, with luminaries like Leonardo da Vinci contributing to the field.[6] In the 1960s tribology rose again to the forefront of government-funded research. Due to limitations in the instrumentation available at the time, the broad interest in tribology then gradually waned. The invention of the atomic force microscope in 1986[7] and its application to friction in 1987[8] may be viewed as the origin of a recent renaissance in tribology.[9,10]

1.1. State of the Art in Materials Tribology

Given tribology's long history and tremendous societal impact, it is somewhat surprising how little mechanistic understanding is available in this field. It has long been recognized, for example, that the complex nature of tribological processes makes it extremely challenging to link nanoscale phenomena to the macroscopic world of gears and engines.[9] On the meso and macro length scales, the elementary mechanisms governing friction and wear, especially for metallic materials, therefore remain elusive. A thorough understanding of the microstructure-properties relation, the key concept of materials science, has not yet been established. Part of the reason is that the microstructure of the material under the contact is highly dynamic[11,12] and its evolution can usually not be observed in situ. This current lack of knowledge makes a strategic tailoring of a material's frictional properties, e.g., during the manufacturing process, very difficult to impossible. Many

Dr. C. Greiner, Dr. J. Gagel, Prof. P. Gumbsch
Institute for Applied Materials (IAM)
Karlsruhe Institute of Technology (KIT)
Kaiserstrasse 12, 76131 Karlsruhe, Germany
E-mail: peter.gumbsch@kit.edu
Dr. C. Greiner, Dr. J. Gagel, Prof. P. Gumbsch
MikroTribologie Centrum µTC
Strasse am Forum 5, 76131 Karlsruhe, Germany
Prof. P. Gumbsch
Fraunhofer IWM
Wöhlerstr. 11, 79194 Freiburg, Germany

engineering systems for this reason rely on a process known as "running-in"[13] to bring a tribological system from the initial to the desired operating state – a process which is in itself barely understood.[14] While tribology has traditionally been a field of study for mechanical engineers dealing with pieces of machinery, such as gears and engines, or for physicists studying tribological contacts on the nanoscale, it is materials science that has the potential to make truly disruptive contributions next, e.g., elucidating the elementary mechanisms governing friction and wear. This makes materials tribology an exciting and emerging field of research.

For metallic tribological contacts most frictional energy dissipation is due to plastic deformation of the subsurface layer.[15] If one of the sliding partners is harder than the other, the softer surface will be ploughed to an appreciable depth by the hard surface's asperities. Thus, the bulk properties of the softer surface determine the friction and wear properties of the entire tribological system.[15] The coefficient of friction (COF) in a sliding system accordingly is expressed as the ratio of the shear strength to the yield pressure of the softer metal.[15] Consequently, the tribological properties of the surface are strongly influenced by the subsurface material and the subsurface microstructure is a function of the plasticity and the nature of the corresponding dislocation activity under a tribological load.[16,17] The subsurface microstructure itself evolves during sliding and may undergo drastic and complex changes during sliding. These microstructural changes as well as the plastic deformation largely determine the frictional forces and the energy required to move the tribological system.

Part of the reason why the microstructure under the contact reacts so strongly are the extreme shear loading that tribologically loaded materials encounter: Large plastic strains and strain gradients[18] accumulate under the contacting surfaces,[19] shear instabilities can trigger shear folding,[20,21] pile-ups and cracks.[22] Together these processes which generally occur in both contacting bodies, may even lead to the mechanically induced mixing of the materials making up the tribological system.[23] These extreme circumstances that are encountered in sliding contacts very often lead to the development of unusual microstructural features; most prominently nanostructured tribofilms directly under the sliding contact and fine grained layers underneath.[24] These layers are believed to be determining the friction and wear performance of metallic contacts and once they are reduced in thickness or removed completely by wear events regenerate while the system is sliding.[25,26]

In this context and for linking the mechanical properties, and consequently the microstructure, of a metal with its tribological properties Argibay and co-workers recently brought forward a feedback cycle.[27] The authors assume that different surface stresses will lead to a variation in how the material responds to shearing, i.e., by grain boundary sliding or by dislocation motion which therefore depend on the normal load during a tribological experiment. To visualize this concept, a feedback loop between grain size, friction coefficient and surface stress was developed which highlights the need to know the stress field under the sliding bodies. In 1983, Hamilton published the analytical expression of the subsurface stress for a sliding spherical contact calculated through a superposition of Hertz's solution and frictional surface traction.[28] Although the stress field

Christian Greiner is a group leader at the Karlsruhe Institute of Technology (KIT). He studied materials science at the University of Stuttgart, where he received his master's degree. For his Ph.D. he worked on bioinspired fibrillary adhesives at the Max-Planck-Institute for Metals Research where he graduated in 2007. He has studied tribological contacts at the nanoscale as a postdoc at the University of Pennsylvania. In 2010, he joined KIT and his research focuses on the elementary mechanisms acting in metals subjected to a tribological load.

Johanna Gagel studied mechanical engineering at the Karlsruhe Institute of Technology (KIT) und graduated with a master's degree in 2014. In her Ph.D. thesis, she investigated dislocation-based plasticity in tribological contacts with simulations and obtained her degree in 2018 at KIT.

Peter Gumbsch is a professor for mechanics of materials at the Karlsruhe Institute of Technology (KIT) and head of the Fraunhofer Institute for Mechanics of Materials IWM. He studied physics and received his doctoral degree in chemistry from the University of Stuttgart in 1991. After a PostDoc at Imperial College in London and the University of Oxford he became a group leader at the Max-Planck-Institute for Metals Research in Stuttgart. His research focuses on modeling and simulation of materials, in particular multiscale modeling approaches with current emphasis on the investigation of friction and wear processes, where complex interactions of mechanics, physics, and chemistry are important.

in a real tribological contact is much more complicated and contains stress singularities from surface roughness and asperities on both contacting surfaces, Hamilton's elastic solution is often a good guidance for the over-all nature of the stress field.

Due to their substantial engineering importance, numerous researchers have contributed to this field of tribology over the

last decades. Briefly and focusing on microstructure research under a tribological loading, one can either start with an annealed, large-grained bulk or a nanograined material. With the large grained samples, the frictional load modifies the material as sketched above. An (ultra-) fine-crystalline tribolayer is formed near the surface and often a layered microstructure evolves.[17,29–31] Starting with a nanocrystalline sample, usually leads to grain growth.[32–34] Recent results however suggest that choosing a stable nanocrystalline alloy—like Pt-Au stabilized by grain boundary segregation—can result in a nanocrystalline material that does not exhibit grain growth even under severe tribological conditions.[35] This structure also shows very low wear rates.[35] With more traditional engineering materials, microstructure evolution and changes in wear properties under a tribological load have been investigated for various initial grain sizes; this includes copper,[17,29,36] steels[37] and cobalt-based alloys.[38] When trying to take a holistic look at the literature, the consensus seems to be that the afore mentioned "tribo-layers" or "third bodies" are observed for many types of contacts and loads.

As far as numerical studies for different friction systems are concerned, molecular dynamic simulations have been employed to model the microstructure changes under a tribological load.[21,39] Among the parameters that were investigated are the sliding speed,[40–42] crystallographic orientation of the surface,[41,42] and existing lattice defects.[41]

Based on these studies, the main processes considered for the microstructure evolution are plastic deformation, mechanical mixing and influence of environment and the counter body.[25,43] Among these processes, dislocation motion can be considered the most important one.[44] Currently, dislocation initiation, their multiplication from pre-existing dislocations and, most importantly, the transport of dislocations under a tribological load are open questions. Previous dislocation modelling results suggest that under a pure indentation and by cross-slip all known features of prismatic dislocation structures can be formed from pre-existing dislocations.[45] This is why both our experimental and our modelling efforts have a focus on dislocation activity.

This brief summary of the scientific context and state of the art in terms of microstructural changes under a tribological load illustrates that due to the complexity inherent to any sliding contact the experiments and models in the existing studies have not yet yielded a satisfactory picture of the elementary mechanisms that lead to microstructure formation and evolution under a contact. This lack of knowledge is most pronounced at the very early stages in the lifetime of a tribological contact. This phase has hitherto been widely neglected in the literature. This is somewhat surprising as it might be there, at the initial tribologically induced shear loading of the metallic sliding partner(s) that the future fate of the materials and thereby the entire tribological system is decided. The study of the onset of microstructural evolution therefore is a first focus of this review, concentrating on dry frictional contacts. As even the most elaborate electron microscopy can only yield a snap shot image of the real microstructure, computer simulations are a vital tool for understanding the elementary mechanisms. Results from dislocation dynamics simulations will therefore also be presented here. The guiding scientific principle spanning this entire body of research is that understanding the microstructure evolution

under a sliding contact and revealing the governing elementary mechanisms in different stages over the lifetime of the contact is sine qua non for being able to strategically tailor materials for reduced friction and wear in the future.

2. Dislocation Transport in Discrete Dislocation Dynamics Simulations

Plastic deformation is crucial for the tribological properties of sliding metal contacts.[44] The mechanisms of this plastic deformation have to be understood to systematically optimize such contacts. While phenomenological models investigating plastic deformation in tribological contacts have been brought forward and have shown their usefulness in applications, a true mechanistic understanding has not yet been achieved. To simplify the inherent complexity of a tribological contact, one may think of a tribological system as a combination of individual asperities indenting and laterally moving over the surface. When such an asperity moves, two processes are expected: First, in the material that has previously not been loaded by the moving counter body, the dislocation density should increase. This is similar to what has been observed for pure indentation.[46] Second, dislocations may be dragged along with the moving asperity as they experience its stress field. Since such a dislocation transport phenomenon may be responsible for a significant amount of plastic deformation and dissipation of frictional energy, they are to be investigated in detail.

The Schmid factor is traditionally used to determine the active slip system, e.g., under a uniaxial stress. For a tribological load this becomes much more complicated as the stress field is very inhomogeneous. Even under the severe simplification of a moving, unlubricated Hertzian contact the Schmid factor strongly depends on the exact location underneath the contact. Additionally, the direction of sliding over a crystal affects the selection of the active glide system.[47] A suitable criterion still needs to be defined to predict the distances over which dislocations are transported on active slip systems in tribological contacts. This question cannot be dealt with by crystal plasticity or other continuum approaches, since such formulations are local in nature and plastic distortion does not depend on the actual transport of dislocations but is simply generated when the stress exceeds locally a critical value. However, dislocation transport can be studied using discrete dislocation dynamics (DDD) or molecular dynamics (MD) simulations. Indentation and sliding have already been investigated by 2D DDD simulations.[48,49] It was found that dislocation mediated plasticity does substantially influence tribological properties and plasticity may even prohibit sliding entirely or at least delay its onset.[49] For a rigid asperity it was reported that the contact area influences friction, contrary to classical friction laws.[48] Down at the atomic scale, the orientation of the crystal and the sliding direction are essential for the evolution of plastic deformation.[50] To slip on a surface with an (111) orientation, dislocations with a Burgers vector parallel to the sliding direction were preferred over others.[51] However, such atomistic simulations impose enormous constraints on dislocation nucleation. Systematically distinguishing between dislocation nucleation and transport is difficult.

For contacts between Cu–Cu, Ni–Ni, or Pd–Pd, the friction coefficient was experimentally found to depend on the direction of sliding.[52,53] The most likely explanation brought forward in the literature for this friction anisotropy goes back to the concept of ploughing versus sliding friction developed by Bowden and Tabor.[15,53] Based on these results, Rigney and Hirth, proposed to combine plastic deformation and friction coefficient.[12a]

We study the transport of dislocations under a sliding contact with a spherical counter body. Such a configuration allows dislocation transport to be separated from nucleation phenomena. This is achieved by moving the spherical tip from a volume with prior dislocation density into an initially dislocation free volume. At stresses well below those necessary for homogeneous nucleation, the moving spherical tip transports dislocations from the dislocation reservoir to the defect free volume. In order to study dislocation network formation, several passes of the tip in the same direction are performed in these simulations.

2.1. Methodology of Discrete Dislocation Dynamics simulations

The general framework for performing 3D DDD for a tribological contact was adapted from the work presented in refs. [54,55] as described in Gagel et al.[56] Each dislocation is gliding within its own glide plane and is represented as a discretized line defect in an otherwise isotropic elastic medium. Dislocations are characterized by their Burgers vector, glide plane normal and line direction. The dislocation line is discretized by a sequence of straight segments, which share nodes. A segment can be arbitrarily oriented within its glide plane. The dislocation motion is restricted to glide. The relevant driving force along the dislocation line is the resolved Peach–Koehler force F_{PK} acting perpendicular to the line direction $F_{PK} = (\sigma n) \cdot b$, where σ is the stress sensor, n is the glide plane normal, and b is the Burgers vector. The local stress tensor is obtained by superpositioning the stress field imposed by boundary conditions, the stresses from the dislocation itself and from all other dislocations. The stress field of the moving spherical indenter is imposed as a boundary condition. The overall displacements, strain as well as a total stresses are calculated following the superposition principle.[57] A second order equation of motion is used to calculated the motion of the nodal points of the dislocation line.[58] The DDD setup investigated for revealing dislocation transport phenomena is visualized in **Figure 1**a.

The configuration investigated consists of a rigid spherical slider performing several unidirectional passes over the surface of a face centered cubic sample. The boundary conditions simulate a single grain within a polycrystalline sample. The embedded grain has dimensions of $10.5 \times 3.4 \times 6.9$ μm³, surrounded by an elastic medium, with exception of the free top surface. Consequently, dislocations can only escape the sample through the top surface while all other boundaries are treated as grain boundaries which dislocations cannot cross. At the very bottom of the elastic medium, the displacement is artificially set to zero. The sides of the elastic medium are treated as traction free.

The following protocol represents a single loading step in the same direction: the spherical tip is placed left to the
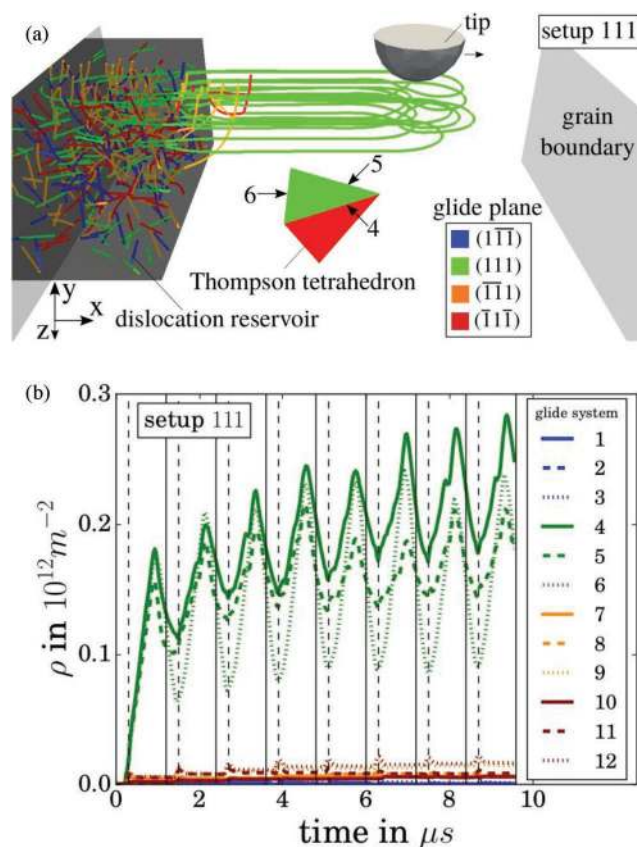

Figure 1. Discrete dislocation dynamics simulations setup for a sliding contact. a) Dislocation structure during the first pass of the sphere (size of sphere not to scale) with (111) glides planes oriented parallel to the surface. b) Dislocation density ρ outside the dislocation reservoir per glide system for eight strokes. The contact is considered frictionless and without cross-slip. a,b) Reproduced with permission.[56] Copyright 2018, Elsevier.

embedded grain and a constant normal force is applied. During one pass, the tip moves toward the right of the sample beyond the right grain boundary reaching a distance of 2.8 μm from the grain boundary. For the next loading step the spherical tip is positioned back at the starting point. By doing so, a gradual increase of the stress field within the embedded grain due to moving indenter is assured. This protocol allows simulating repeated unidirectional tribological loading.

To study dislocation transport phenomena, a "dislocation reservoir" of $2.6 \times 2.6 \times 5.2$ μm³ in size was placed at the left side of the embedded single crystal. The rest of the embedded grain's subvolume initially was dislocation free. This artificial configuration was chosen in order to provide different dislocation sources, while allowing the dislocations initially situated in the reservoir to glide into the rest of the material without obstacles or other constraints. The initial sources are of Frank-Read type and are statistically distributed as far as their Burgers vectors, length, position and orientation are concerned. In order to simulate a solid solution strengthened material, a critical lattice friction stress τ_r for the onset of dislocation glide is introduced. Once the absolute value of the resolved shear stress is higher than τ_r, the dislocations start to move. Once a dislocation

1806705 (4 of 19)

does glide, the resolved shear stress acting along the dislocation is lowered by τ_r. In the case of the simulations presented here, τ_r corresponds to a value of 10 MPa as it is found when adding one atomic percent of manganese or magnesium to aluminum.[59] We chose a solid solution strengthen material to increase the critical resolved shear stress to stabilize—among other things—the dislocation structure after unloading. This phenomenon will be more pronounced in our overall low dislocation density simulations compared to real-life materials where dislocation reactions will increase the stability of transported dislocations.

Herein, a 111 setup consisting of a $[\overline{1}\overline{1}1]$ indentation and a $[\overline{2}11]$ sliding direction is described. The directions are given with respect to the crystals coordinate system. To indicate that one of the six possible Burgers vectors is oriented parallel to the sliding direction, the index ()$_{par}$ is used. For the 111$_{par}$ scenario, the indentation direction is $[\overline{1}\overline{1}1]$ and the sphere sliding in $[\overline{1}01]$. A detailed discussion of dislocation transport for different crystallographic orientations and sliding directions can be found in ref [56].

Indentation is performed parallel to the negative y-axis of a lab coordinate system while sliding is parallel to this lab coordinate system's positive x-axis. The Hamilton solution is applied to calculate the contact stresses both in the bulk and the surface.[28]

In order to calculate the total resolved Peach–Koehler force and for mimicking constant load boundary conditions, the Hamilton stress field is calculated for a given normal force and then added to the total local stresses. The forces acting on each dislocation node are computed by integrating the Peach–Koehler forces acting along each segment connected by this node.[55] In order to decrease the calculation time and instead of highly refined FEM meshes, the analytical solution for the stress field under the moving sphere was used. It was possible to apply a rather course volumetric discretization. To more accurately reproduce the glide of dislocation nodes located at the surface, an image construction for those dislocations piercing through the surface is implemented. The following loading parameters for simulating the sliding contact are chosen: Normal force $F_y = 400$ µN, sphere radius $R = 120$ µm and a sliding velocity v_x of 12 m s^{-1}.

For simulating the behavior of aluminum under a sliding contact, a lattice constant $a = 0.404$ nm, shear modulus $G = 27$ GPa, Poisson ration $v = 0.347$, solid solution strengthening stress $\tau_r = 10$ MPa and initial dislocation densities in the dislocation reservoir of $\rho_1 = 5 \times 10^{12}$ m^{-2} (sources distributed on twelve glide systems) and $\rho_2 = 2.5 \times 10^{12}$ m^{-2} (sources distributed on three glide systems) are used. The contact coefficient of friction was set to zero. Assuming a purely Hertzian contact, these loading conditions result in a contact radius of roughly 760 nm, an elastic indentation depth of about 5 nm, a maximum elastic shear stress of 100 MPa, and a maximum Hertzian contact pressure of 330 MPa. When visualizing the results, dislocation structures are colored according to their glide plane.

2.2. Results

Without cross-slip and for a friction coefficient of zero with the glide systems being fully populated and ρ_1 being the dislocation density in the reservoir, for each pass of the spherical tip, the dislocation density within the dislocation reservoir and for all glide systems increases. For the 111 and the 111$_{par}$ setup, dislocations are transported on glide planes parallel to the surface. Glide systems are activated where one of the three Burgers vectors is either perpendicular—the 111 case—or parallel—the 111$_{par}$ case—to the sliding direction.

Once the sphere starts to glide on the initially dislocation free volume, only certain glide systems are being activated. The dislocation density within the reservoir either remains constant or slightly decreases once the spherical tip has crossed the border between the reservoir and the initially dislocation free subvolume. This situation is visualized in Figure 1.

Figure 1a shows a situation during the first pass of the sphere for the 111 setup. Within the initially dislocation free volume, dislocations are only transported on (111) glide planes. Specifically, Burgers vectors of $[\overline{1}01]$, $[\overline{1}10]$, and $[01\overline{1}]$—denoted by their glide system numbers 4, 5, and 6 in the Thomson tetrahedron respectively—were chosen for dislocation transport.

The evolution of the dislocation density over time and for each of the twelve glide systems possible for fcc materials is plotted in Figure 1b for the 111 setup. In this figure, eight individual and unidirectional passes of the sphere are captured. These passes are highlighted by solid vertical lines. The broken vertical lines indicate the point in time where the sphere passes the boundary between the dislocation reservoir and the initially dislocation free volume. For each pass of the sphere, the dislocation density increases. This is true for all three of the above mentioned glide systems, again referred to as 4, 5, and 6. These results are the average of a total of 16 simulations, all of which having an initially statistically equivalent dislocation density and structure. During the time the sphere is in contact with the dislocation reservoir, the dislocation density in the initially dislocation free volume relaxes. This either happens through dislocations sliding back into the direction of the dislocation reservoir, or by other phenomena leading to a reduction in dislocation density. The dislocation structure cannot relax completely reaching an equilibrium state, as before a steady-state is reached, the tip performs the next pass and dislocations are again multiplied and transported out of the dislocation reservoir. The dislocation density within this initially dislocation free volume and on all three selected glide systems oscillates between each individual pass and the relaxation that follows, while overall an increase in dislocation density is observed. For glide system 6, having a $[01\overline{1}]$ Burgers vector and thereby being perpendicular to the direction of sliding, these oscillations are most pronounced. In a 111$_{par}$ setup, these oscillations were found to be the smallest for dislocations having a Burgers vector parallel to the sliding direction.[56] Here, dislocation transport is observed on the inclined $(\overline{1}1\overline{1})$ glide plane, which contains the sliding direction.[56]

Analyzing the surface topography that is associated with these dislocation transport phenomena we found, that it differs in and outside the dislocation reservoir once the sphere starts to slide. Slip traces might emerge on the surface, as they have also been reported experimentally.[60] It is obvious, that slip traces require a Burgers vector with nonzero components along the surface normal. In case of the 111 setup, transport occurs only
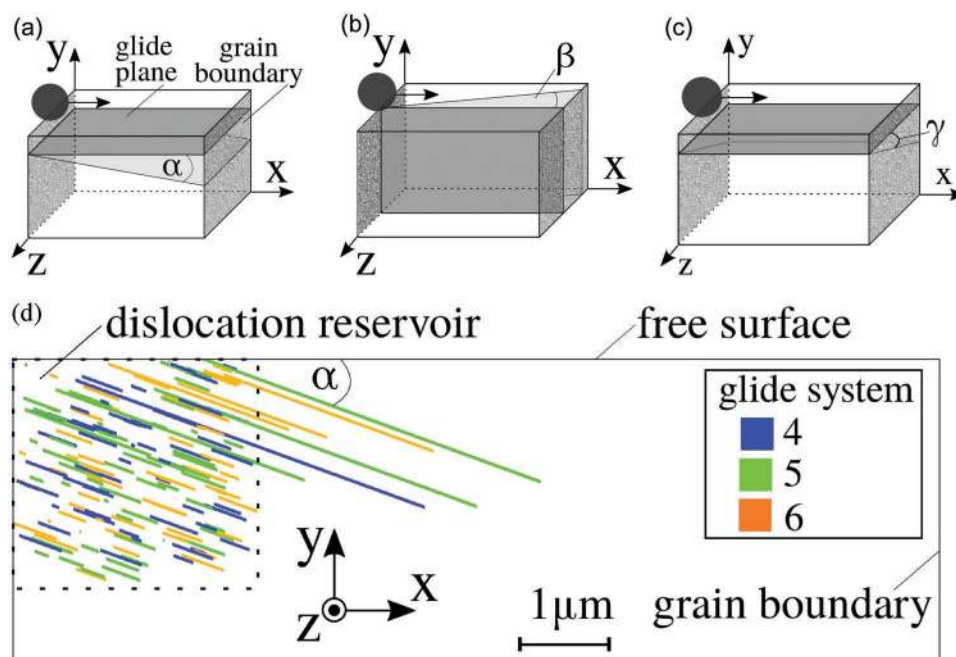
Figure 2. Different glide plane orientations and inclinations. a) Glide plane rotation around the z-axis, angle α; b) glide plane rotation around the y-axis, angle β; c) glide plane rotation around the x-axis, angle γ. d) Dislocation structure after one pass of the sphere for the glide planes rotated by $\alpha = -20°$. a–d) Reproduced with permission.[56] Copyright 2018, Elsevier.

on 111 planes, thus no surface slip traces occur. For the 111_{par} setup, only the dislocation transport observed on inclined $(\bar{1}11)$ glide planes—or more specifically the respective glide systems having also a Burgers vector inclined to the surface normal—lead to surface traces.

Similar dislocation transport phenomena into the initially dislocation free volume were also observed when in a more comprehensive study all the initial setups were considered.[56]

Upon activating cross-slip but still considering the contact as frictionless, the dislocation density being introduced in the initially dislocation free volume through the moving sphere is higher compared to the non-cross-slip situation for the 111_{par} case. Generally, the same glide systems are being chosen for transport as without cross-slip. When a friction coefficient of 0.25 is taking into account and cross-slip is again not considered, dislocations are being transported on the same glide systems as for the other two scenarios.[56] This demonstrates that the selection of glide systems seems not to be overly sensitive to either cross-slip phenomena or the exact value of the friction coefficient. The same is true for the surface topography as well as for the dislocation microstructure having evolved after several passes of the moving sphere. However, the dislocation density slightly increases for friction coefficients larger than zero. This is in agreement with what one would expect as higher friction coefficients will lead to more dislocation activity.

Another interesting phenomenon that can very elegantly be investigated by dislocation dynamics simulations is the nonlocal nature of plastic deformation by measuring how far dislocations are being transported under the moving tip.[56] We therefore studied this transport length Δx for a frictionless contact and without cross-slip. The transport length Δx is defined as the maximum distance a dislocation moved outside the dislocation reservoir for each glide plane per glide system and for each individual pass of the sphere. As in DDD simulations dislocation sources are being statistically distributed, this arbitrary source distribution might lead to artefacts when determining Δx. We ruled out such an effect by averaging over 30 statistically comparable simulations. These dislocation sources are of Frank-Read type on a specific set of glide planes. This insured that the determined Δx value is not influenced by artefacts through reactions with dislocations populating other glide planes. Three different glide plane orientations are analyzed, shown in **Figure 2**a–c, for a frictionless contact without cross-slip. For these investigations, the dislocations within the reservoir initially only populate the glide planes parallel to the ones highlighted in Figure 2a–c.

In this picture, the xz-glide plane is oriented parallel to the sliding interface. The glide plane can be inclined around the z-axis by angles α and γ, or around the other axes of the coordinate system and by increasing the respective angles α, β, or γ, as depicted in Figure 2. Populating only the (111) planes and for $\alpha = \beta = 0°$, corresponds to both the 111 and the 111_{par} setup. Once the sphere starts moving, dislocation sources are being activated, dislocations are bowing out, leading to drawn-out dislocation loops following the sliding sphere. Figure 2d visualizes such a configuration for an initial 111 setup inclined around the z-axis by −20°. The numbers referencing the glide systems correspond to the ones defined above. For this scenario, the Burgers vector of glide system 6—$[01\bar{1}]$—is perpendicular to the direction of the passing sphere. Plotting the maximum transport length Δx as a function of the angles α, β, γ results in **Figure 3**.

For a configuration without any inclination—$\alpha = \beta = \gamma = 0°$—the Burgers vector of the dislocations does not matter and
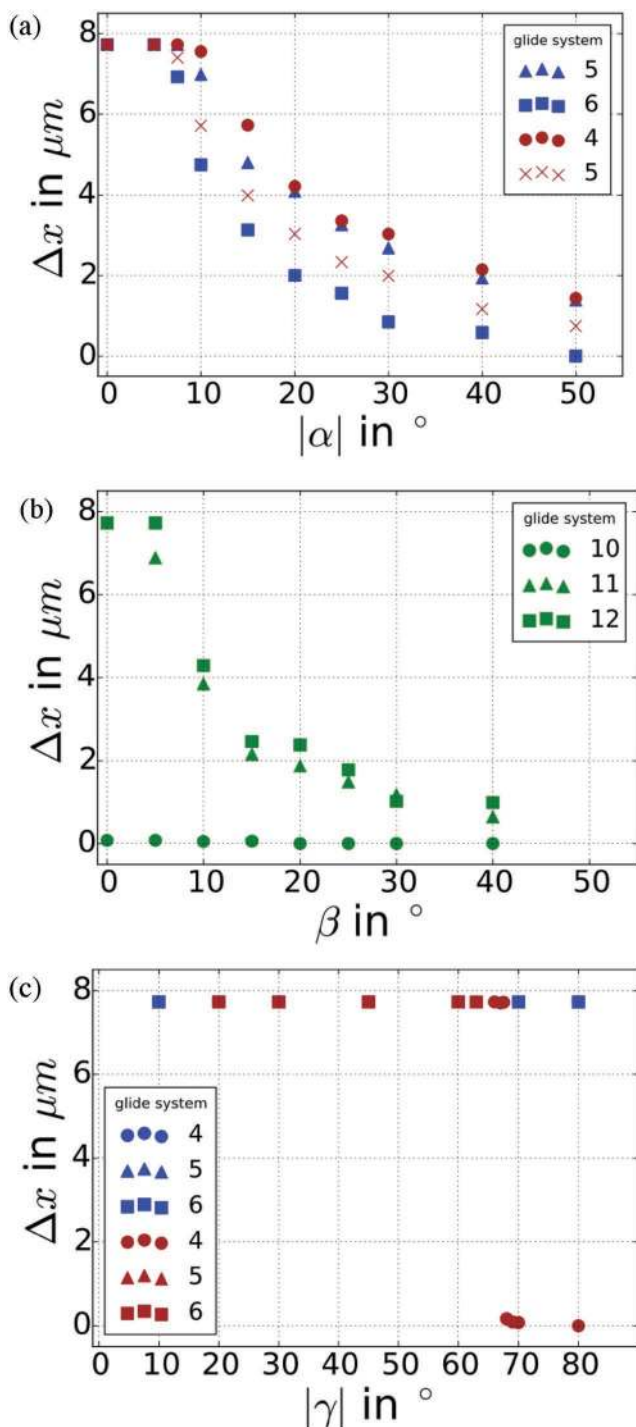
**ADVANCED
SCIENCE NEWS**

www.advancedsciencenews.com

**ADVANCED
MATERIALS**

www.advmat.de

Figure 3. The maximum distance Δx dislocations are being transported by the moving sphere as a function of glide plane and Burgers vector orientation. a) For a rotation around the x-axis by angle α. Blue data points refer to setup 111 and brown ones to 111_{par}. b) For a rotation around the y-axis by angle β and for a 121_{par} setup. c) For a rotation around the z-axis by angle γ. Blue data points refer to setup 111 and brown ones to 111_{par}. a–c) Reproduced with permission.[56] Copyright 2018, Elsevier.

all dislocations are being completely transported through the initially dislocation free volume. A more detailed investigation has shown that one exception to this broad statement has to

be made: For a 121_{par} setup one glide system was found where independent of β, no dislocations were transported at all.[56] Figure 3 demonstrates that for increasing α and β the maximum length Δx dislocations are being transported decreases. A rotation around the axis parallel to the sliding direction—angle γ—seems not to influence the transport length. For positive values for the angle α, dislocations get transported less compared to negative ones, as they leave the material through the free surface/sliding interface.

2.3. Discussion

Taking a holistic view, these DDD simulations demonstrate that dislocations are following the passing sphere and thereby being transported out of the dislocation reservoir and into the initial defect free volume. In order for this to happen, two conditions must by fulfilled: there must be a sufficiently high driving force for dislocation glide and the dislocation must be able to follow on its glide plane or possibly cross-slip plane the moving indenter tip. For a given orientation of the crystal, the sliding direction can be the deciding factor whether dislocations are being selected for transport or not. The choice of the activated glide system is based on the orientations of the Burgers vector and the glide plane normal. In order for dislocations being transported over a long distance, a positive driving force has to act at best parallel to the direction of the passing sphere and the dislocations have to be able to follow the sphere geometrically. An extremely unfavorable scenario for this to happen is when the glide planes are oriented normal to the sliding direction: dislocations are not transported at all with the sphere. A criterion for which glide planes are being chosen for dislocation transport can be formulated.[56]

To characterize the driving force on dislocations in each glide system, a volume underneath the indenter is identified where the resolved shear stress exceeds a critical shear stress. This defines an isostress surface for a volume within which dislocation glide may occur. For the tribological contact of a spherical indenter moving over a planar fcc metal, Gagel et al. suggested an analysis based on the analytical Hamilton solution, which makes it possible to identify the glide systems that facilitate dislocation transport.[56]

Upon sliding this indenter laterally, the stress field moves with the position of the tip and dislocations in the subsurface volume under the moving sphere start to glide when the resolved shear stress exceeds the lattice friction stress τ_r. Relying on the analytical Hamilton solution, isosurfaces for $\tau = \tau_r$ are calculated for each glide system, followed by projecting them onto a plane perpendicular to the direction of the sliding sphere. By comparing the area of these geometrical cross-sections for each glide system, and counting overlapping areas only once, a stress criterion is developed. This concept only defines the effective area for a high enough driving force, but does not take into account whether dislocations on these glide systems are able to follow the sliding tip from a geometrical point of view. To resolve this issue, the stress field and glide plane orientation criterion are combined. This is exactly what was performed in our simulations with the details being described in ref. [56].

**ADVANCED
SCIENCE NEWS**
www.advancedsciencenews.com

**ADVANCED
MATERIALS**
www.advmat.de

As far as dislocation transport is concerned, when the glide plane is oriented parallel to the surface, dislocations up to a certain distance from the indenter tip (defined by the projected area) follow the tip completely through the simulated volume. In cases where one of the six Burgers vectors is parallel to the sliding direction, e.g., in the 111_{par} case, also dislocations moving on glide planes inclined to the sliding surface, but containing the direction of the moving sphere, are able to follow the tip throughout the entire initially dislocation free volume. On these inclined glide planes, only two out of three glide systems are selected for dislocation transport. This DDD-based result is in complete agreement with purely geometrical considerations based on the cross-sectional area of these glide systems. The cross-sectional areas' size—as being determined for each glide system—correlates with whether dislocations are being transported on them or not. This shows that it is possible to identify active glide systems for dislocation transport by combining the resolved shear stress and glide plane geometry conditions. When deriving these criteria, certain simplifications had to be made. How to exactly define the critical size of the geometrical cross-sectional area remains to be discussed and investigated further. It also has to be considered that the normal force, the friction coefficient and the size of the sphere change the position and the shape of the stress field. Not all of these factors might have been taking into account sufficiently in the current state of our simulations. One might hypothesize for example that in cases the geometrical cross-sectional shape of the stress field branches out or possesses increased complexity due to other factors, then dislocations might be forced to bow out more, thereby making dislocation transport less likely.

The more the glide plane normal diverges from being perpendicular to the sliding direction, the earlier dislocations start to no longer glide with the spherical tip and contact stresses are not sufficient for dislocation transport. Relying on the geometrical cross-section allows to formulate a geometrical criterion to evaluate the maximum possible transport length Δx for dislocations on a specific glide system. The geometrical cross-section defines a volume and with this volume the glide plane intersect and form an intersection line. Along this intersection line there is a maximum coordinate in sliding direction and this corresponds to the maximum transport distance possible for a dislocation. Owing to the generally complicated geometrical cross-sectional shapes associated with the glide systems for almost all dislocations, these intersection points are unique for each individual glide system.

The free surface associated with the tribological contact can also act as a restriction to how far dislocations can be transported. For example, when the glide plane is misoriented around the z-axis (angle $\alpha \neq 0$), dislocations are transported less as they intersect with the free surface before having reached the end of the initially dislocation free volume. Depending on the exact situation, this might however not be true for rotations around all three axes.[56]

When cross-slip is possible, the number of geometrical options available for the dislocations to glide and follow the moving sphere is increased. A dislocation may even choose to cross-slip back and forth between different glide planes, thereby allowing it to reach longer dislocation transport distances. In this case, both of these glide planes might not necessarily be parallel to the path of the moving sphere, but the resulting overall direction of dislocation transport is. In order to activate such a motion, also with cross-slip, a sufficiently high resolved shear stress is necessary. This is why not all dislocations that might geometrically be able to follow the sliding sphere are indeed transported.

For a tribological contact consisting of a moving sphere, it seems that those dislocations are chosen to glide first that shear the material in sliding direction and further into the subsurface bulk material. Our DDD simulations indicate that these dislocations are able to follow the moving sphere the easiest. This is in contrast to the results previously obtained for pure indentation.[45] Our future research will need to shed more light on why this is, as well as take into account what happens when dislocations are being transported into a subvolume of material that is not initially dislocation free. Such a configuration most likely will lead to additional dislocation reactions that might impede or favor the transport and multiplication of dislocations under the severe stress conditions imposed by a tribological load. The same goes for a more detailed study for how friction coefficients above zero might change the results presented and discussed above.

3. Initial Sliding Contact

Since dislocation transport is such an intricate problem to study, even sophisticated simulations as the ones presented above, are not yet able to answer the question why so often a layered subsurface microstructure is observed under the extreme shear imposed by a tribological load. We therefore approached this problem experimentally.[61] In order to do so, we focused our attention at the very early stages of a dry sliding contact.

The materials and methods for this research are described in more detail in the Supporting Information and in ref [61]. In short, polycrystalline high-purity oxygen-free (OFHC) copper was brought into contact with sapphire spheres with a diameter of 10 mm. To reduce the complexity inherent to any tribological experiment, we did not lubricate the experiment and chose a mild normal load of 2 N, resulting in a nominal Hertzian contact pressure of about 560 MPa. The structural transformations were examined using a focused ion beam/scanning electron dual beam (Helios NanoLab 650) and an FEI Titan³ 80–300 transmission electron microscope (TEM). For all TEM foils, a cross-sectional view, parallel to the sliding direction and in the middle of the wear track were chosen. Detailed crystallographic information was obtained from Transmission Kikuchi diffraction (TKD).[62] The density of geometrically necessary dislocations (GND) can be determined based on the misorienation data gathered by TKD, or electron backscatter diffraction (EBSD).[63] This is based on the distance between the two points used to calculate the misorientation and the length of the Burgers vector of a ½⟨110⟩ dislocation (0.255 nm for copper), being the most common perfect dislocation in a fcc crystal. The GND density is correlated with a misorientation tilt angle, regardless of slip system.

3.1. Results and Discussion

When investigating the cross-sectional microstructure after one single pass by TEM, we observed the formation of a distinct
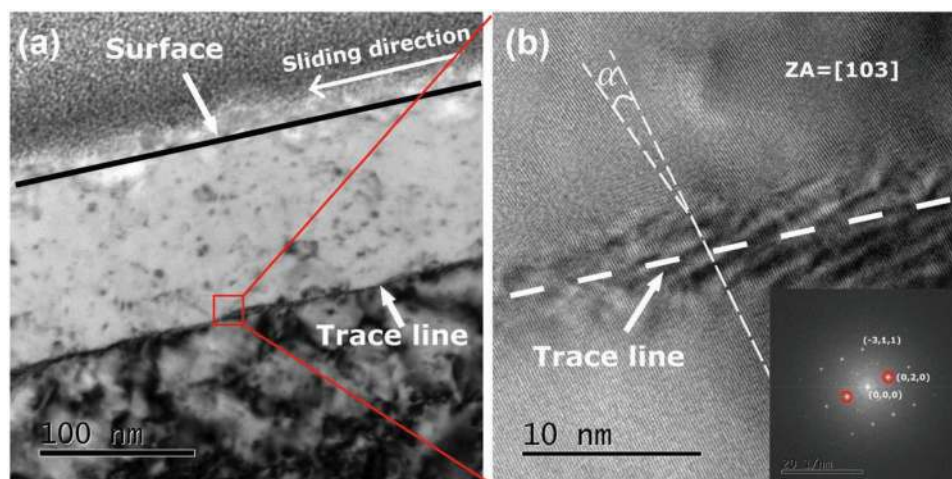
Figure 4. Transmission electron microscopy of the subsurface microstructure after one, single sliding pass. a) TEM bright-field image for a 2 N normal load wear track; b) high-resolution TEM image of the trace line in the red rectangle area of (a), with the fast Fourier transform image of the lattice beneath the trace line in the bottom-right corner. The TEM foil was prepared perpendicular to the sliding surface (cross-section) and along the sliding direction. a,b) Reproduced with permission.[61] Copyright 2018, Elsevier.

microstructural discontinuity already after a single (unidirectional) pass of the sapphire sphere, see **Figure 4**.

The origin of the line-like contrast observed in Figure 4a is not obvious but its occurrence is highly reproducible. Based on TKD scans over the line we measured an average misorientation of 4.6 ° between the material above and below. Therefore, the line-like feature effectively has the character of a small angle grain boundary. High-resolution transmission electron microscopy (HRTEM) shown in Figure 4b demonstrates the tilt character of the line. In all of these images the depth of this line-like feature und the contact is at about 150 nm under the surface and the part of the material above the line appears with brighter contrast compared to the material below. This brighter contrast may be interpreted as a lower density of dislocations above the line. For the image presented in Figure 4b, the zone axis (ZA) is a [103] direction, as determined from the fast Fourier transform image of the area beneath the line. Therefore, the lattice planes visible in this image have a {200} and are rotated by 7.9° at the location of the line-like contrast. The images shown in Figure 4 strongly suggest that the line consists of dislocations and in contrast to a classical small angle grain boundary has a width of ≈5–8 nm. It effectively has the character of a small angle grain boundary while it seems to be a much more complex network of self-organized dislocations (having a variety of Burgers vectors). To probe the hypothesis that the line has the character of a small angle grain boundary, one can apply the classical model of a small angle tilt boundary consisting of edge dislocations.[64] When doing so and assuming that in copper an array of ½⟨110⟩ dislocations will make up such a tilt boundary, an average spacing of 1.8 nm is calculated when using the measured rotation angle of 7.9°. By taking into account the zone axis of the experimentally investigated TEM foil and then projecting only the edge component of the ⟨110⟩ dislocations on to the (103) crystallographic plane, we experimentally determined an average dislocations spacing in our TEM foil of 1.5 nm. This excellent agreement between a simple model description and our experimental results further substantiates that the line

feature can be thought of as a small angle grain boundary with increased complexity.

Having settled on what this line-like feature—from now on referred to as dislocation trace line—is, the question remains how to explain this dislocation self-organization phenomenon. Among the different candidates of plausible explanations the one that has proven to be most successful is to look at how dislocations move under the stress field of the moving sphere (very similar to the DDD analysis presented above). Before we do so, it should be mentioned, that other causes like a possible material transfer to the sapphire sphere and back onto the copper sample could not be supported by the experimental results since we did not find any Cu signal in X-ray photoelectron spectroscopy measurements on the sapphire spheres.[61] We also did not find any evidence for chemical changes in the subsurface area, investigated by TEM-based electron energy-dispersive X-ray spectroscopy (EDXS). The contrast changes observed in Figure 4 therefore most likely stem from differences in dislocation density and not in chemical composition.

This being said, let us come back to the question how this dislocation organization phenomenon can be explained. We hypothesize that the main contribution to the forces acting on the dislocations and making them move in the cross-sectional area underneath the sliding sphere, is the in plane shear component σ_{xz} of the stress field as calculated by Hamilton.[28] We therefore visualize this shear component as presented in **Figure 5**.

Without limiting the generality of the argument we limit the discussion of the action of the stress field on the different possible dislocations to four, perpendicular, slip systems underneath the moving sphere. Dislocations on all four systems are assumed to exist in the material when the sliding sphere approaches. In this picture, the dislocations with a Burgers vector oriented parallel to the surface either follow the sphere or are left behind. The dislocations with Burgers vectors perpendicular to the sliding surface are either pushed further into the bulk of the specimen or pulled to the surface,
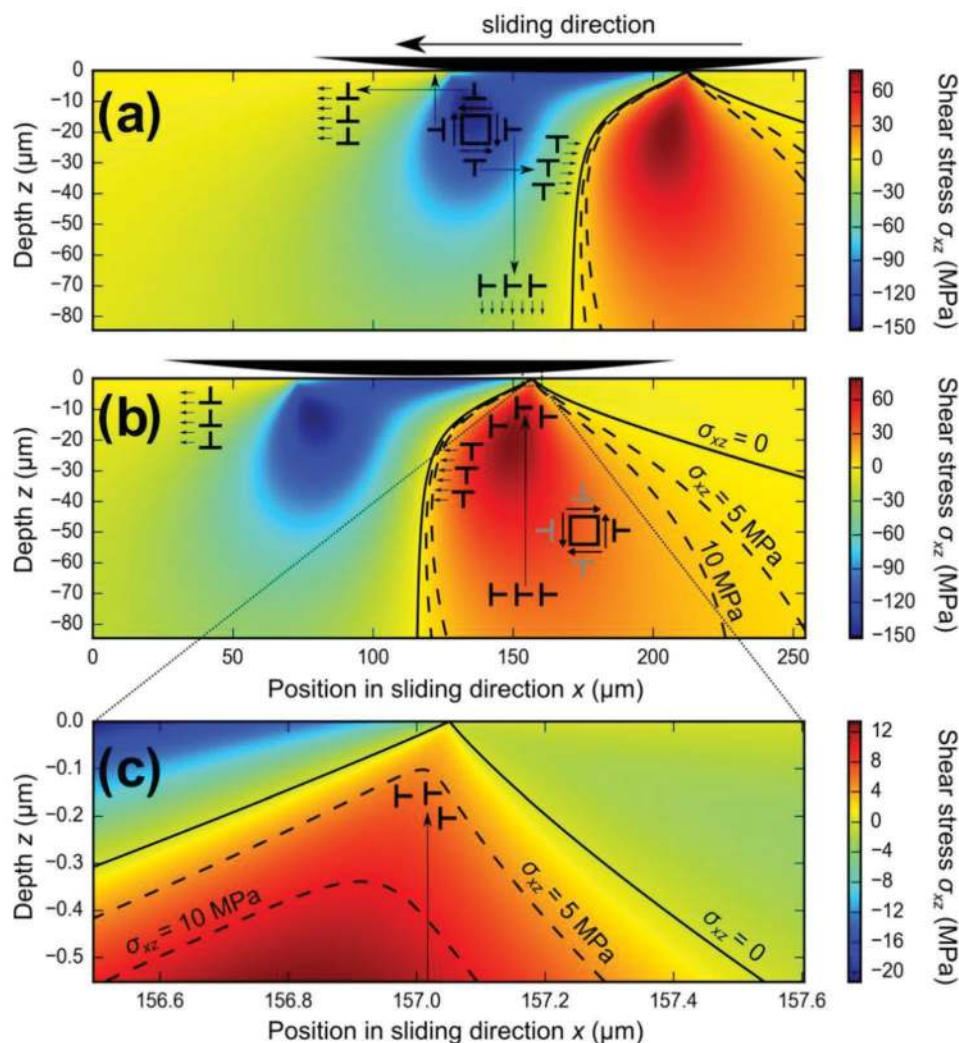
ADVANCED
SCIENCE NEWS
www.advancedsciencenews.com

ADVANCED
MATERIALS
www.advmat.de

Figure 5. Visualization of the stress field under the moving sapphire sphere. We chose the *xz*-component of the stress field for the experimentally determined friction coefficient *μ* = 0.25. Sliding is in negative *x*-direction. Solid and broken lines show contours of constant stress. (a) and (b) display the same stress field but translated by the motion of the sphere. The arrows indicate the movement of the respective dislocations. (c) is a zoom-in of the near-surface region at the trailing edge of the contact. a–c) Reproduced with permission.[61] Copyright 2018, Elsevier.

where they leave the sample. The latter can explain the area of reduced dislocation density above the dislocation trace line as observed in the electron microscopy images presented in Figure 4.

The sphere is not indenting the surface but sliding, and as the stress field has a sign change below the sliding indenter, indicated by the solid line in Figure 5, certain dislocations that first had moved into the bulk of the specimen later are pulled up again toward the surface, as sliding progresses (Figure 5b). The question then is how far the dislocations are moving toward the surface. Depending on the friction coefficient, at the trailing edge of the moving sphere, the σ_{xz} stresses go to zero underneath the contact. The dislocations therefore will stop moving toward the surface before they reach this point. Probably it is reasonable to assume that a minimum yield stress is needed to move dislocations in high-purity copper. The absolute value for this stress is expected to range between the Peierls stress for a well-annealed copper

single crystal—≈1 MPa—and a yield stress of several hundred MPa, as it was reported for pure copper, depending on work hardening and dislocation density.[65] Based on literature results, it seems that a value between 5 and 10 MPa is a reasonable estimate for the minimum stress necessary to move a dislocation in annealed copper. For the contacting materials used in our experiments and for the experimentally measured friction coefficient of 0.25, Figure 5b shows isostress lines for both values. As can be seen in the zoom in view of the stress field presented in Figure 5c and taking the conservative value of 5 MPa, dislocations are expected to stop moving toward the surface somewhere between 100 and 200 nm under the contact. This is precisely where we experimentally observe the dislocation trace line (see Figure 4). It therefore stands to reason that due to the complex stress field of the moving sphere, edge dislocations of a certain orientation are initially pushed deeper into the bulk of the material. As the sphere keeps moving, these dislocations are pulled up again toward the sliding

ADVANCED
SCIENCE NEWS
www.advancedsciencenews.com

ADVANCED
MATERIALS
www.advmat.de

contact where they stop roughly 150 nm under the surface and self-organize into a complex dislocation network. This network manifests itself as a line-like feature in cross-sectional TEM images and effectively has the character of a small angle grain boundary. These dislocations exactly have the Burgers that leads to the observed forward tilt of the lattice planes shown in Figure 4. A more detailed analysis applying this contact stress based model description yielded that the depth of the trace line only has a very weak dependency on the friction coefficient and on the normal load.[61] The effect of different materials other than copper and of other crystallographic orientation were experimentally tested and could successfully be described by this model.[61] The ubiquitous generation of such a dislocation trace line during the very first trace means that the foundation for any future microstructure evolution or microstructural discontinuity in a material subjected to tribological loading is laid during the very first sliding pass. A remaining open question and a topic of ongoing research is the exact 3D-structure of the dislocation network constituting the trace line and how dislocations emitted from the surface contribute to its formation.

4. Multiple Passes and Higher Normal Loads

With strong experimental evidence for what happens during the very initial stages in the lifetime of a metallic tribological contact, the question naturally follows how the material reacts to the severe conditions imposed for an increasing number of sliding cycles. We studied this with the same set up as described above and a systematic increase in the number of passes of the sapphire sphere over the high-purity copper samples.[61]

Experimental results from scanning transmission electron microscopy (STEM) investigations on samples subjected to two, four, six, and ten passes are presented in **Figure 6**.

As expected, in all of these images the same horizontal line-like contrast was found as introduced in the paragraph above and explained by the contact mechanics model. Once the number of passes exceeds ten, a second dislocation trace line is observed in the STEM images. The appearance of a second line-like feature was also found for higher normal loads.[61] In both cases the second trace line could so far not successfully be explained.

Applying the contact stress model nonetheless, one would not expect an increase of the depth of the dislocation trace line
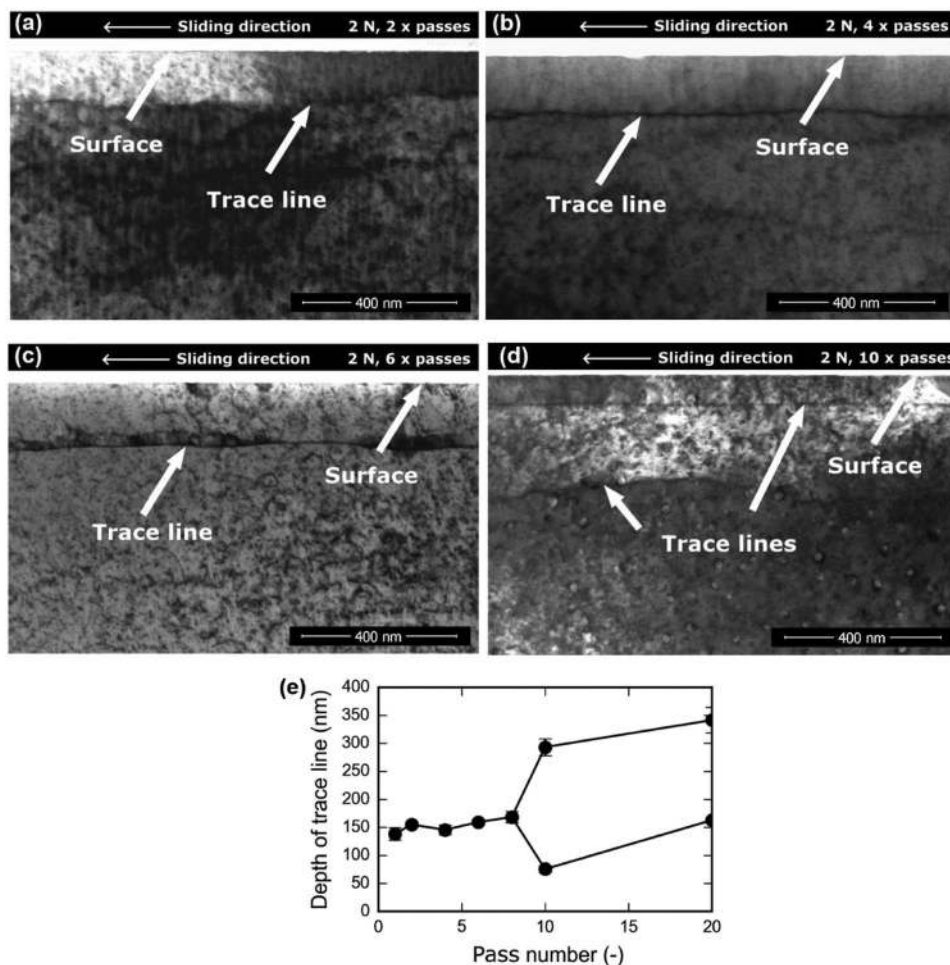

Figure 6. Scanning transmission electron microscopy images for different numbers of unidirectional passes. a) 2 N, 2 passes; b) 2 N, 4 passes; c) 2 N, 6 passes; d) 2 N, 10 passes. e) The depth of the dislocation trace lines plotted as a function of the number of passes for a load of 2 N. All foils were prepared perpendicular to the sliding surface (cross-sections) and along the sliding direction. The bright contrast at the very top of the images is caused by the protective platinum layer. a–e) Reproduced with permission.[61] Copyright 2018, Elsevier.
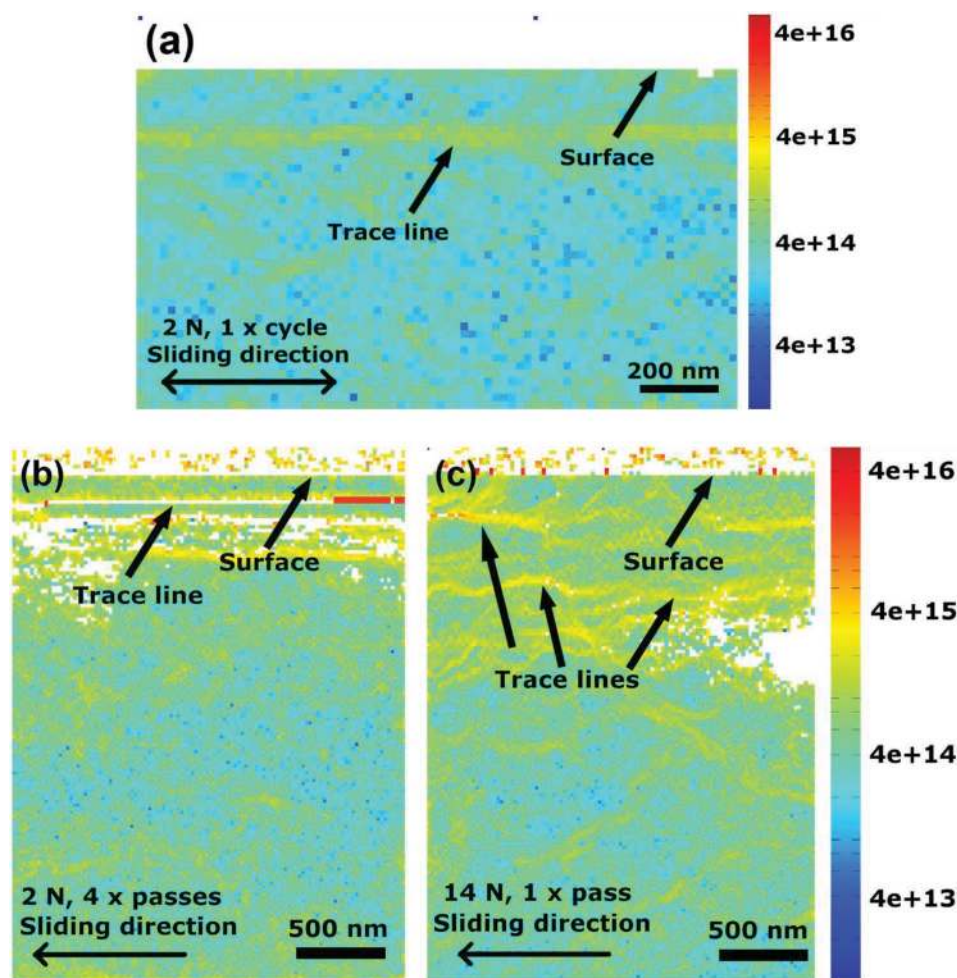
**ADVANCED
SCIENCE NEWS**

www.advancedsciencenews.com

**ADVANCED
MATERIALS**

www.advmat.de

Figure 7. Transmission Kikuchi diffraction based misorientation analysis. Misorientation interpreted as density of geometrically necessary dislocations: a) for a normal load of 2 N, trace and retrace; b) 2 N normal load, four passes; c) 14 N normal load, single pass. The color bar gives the number of GNDs per unit area in m². a–c) Reproduced with permission.[61] Copyright 2018, Elsevier.

with the cycle number. The experimental results are presented in Figure 6e, where the average depth of the trace line is plotted as a function of the number of passes and confirming this hypothesis.

One could however argue that for several passes in the same direction the misorientation at the trace line should increase. We probed this by performing four passes in the same direction and then determined the misorientation angle via TKD (**Figure 7**).

The angle measured is 15.4°, which is significantly more than after only one pass and again in agreement with how we expect dislocations to move and self-organize.

It should also be pointed out that in all of these cases we did observe the dislocation trace line, even though with an increasing number of passes also the amount of nonindexed pixels in its vicinity increased. The same is true when a higher normal load was chosen. An example for a TKD measurement for a sample loaded with 14 N and after a single pass of the sapphire sphere is presented in Figure 7c. As for the STEM for higher cycle numbers,[61] multiple trace lines were found in the subsurface area.

When comparing the influence of different normal loads and pass numbers, one finds that the depth of the trace line is always at around 120 nm and in virtually all cases exactly parallel to the sliding surface. Once a certain threshold is reached, secondary and tertiary trace lines are formed, most probably in order to accommodate the further increase in dislocation density. Up to this limit, our hypothesis for how dislocations move in the inhomogeneous stress field under the moving sphere is able to predict the experimental results with high accuracy. The initiation of the microstructural changes found in metals under tribological loading, while certainly not fully understood yet, have been evaluated to a significant extent.

5. Cyclic Loading and Microstructure Evolution

Our model description predicts that on a retrace of the sapphire sphere, dislocations of the opposite Burgers vector are pulled from the bulk of the material to where the trace line has formed during the initial pass of the sphere. Thereby the tilt angle associated with the dislocation trace line should decrease.

**ADVANCED
SCIENCE NEWS**
www.advancedsciencenews.com

**ADVANCED
MATERIALS**
www.advmat.de

Theoretically, the trace line might even vanish, but due to irreversible dislocation reactions this seems quite implausible. One would consequently not expect the trace line to be annihilated completely upon a retrace, but the misorienation angle should be drastically reduced. When testing this hypothesis experimentally and measuring the misorientation angle with TKD after a trace and retrace and for a normal load of 2 N, the results presented in Figure 7a were found. The misorientation analysis resulted in an angle of 0.6° between the material above and below the trace line. The misorientation therefore is not zero, but significantly smaller than for just one trace; in complete agreement with our contact stress based hypothesis.

As summarized in the introductory paragraph, the majority of the existing literature focuses on late stages of microstructural changes under a tribological load. A fundamental understanding of the elementary mechanisms acting at different stages of the microstructural evolution is still lacking. This is why we started a series of systematic experiments investigating the subsurface structural transformations during different stages in the lifetime of a tribological contact. The same model system was chosen as above: High-purity copper tested against sapphire spheres in a reciprocating fashion. The only variable was the sliding cycle number that was increased from 1, 10, 100, 500, 1000, up to 5000 cycles. All other parameters were kept constant and as outlined at the beginning of Section 3. The microstructural investigations were based on focused ion beam (FIB) and scanning electron microscopy (SEM) in combination with cross-sectional EBSD.[66]

Focused ion beam cross-sections for all cycle numbers from the middle of the wear tracks are presented as cross-sectional SEM images in **Figure 8**.

No contrast features at the surface are observed in the unloaded material (Figure 8a). After ten sliding cycles a slight contrast change in the subsurface area is seen in Figure 8b. The thickness of this tribologically infused microstructural change is $0.52 \pm 0.19\,\mu m$. This thickness is defined as the distance from the sliding surface to where the contrast no longer changes in the subsurface area. On any image used for this thickness determination this measurement was repeated five times at different locations. The average value and standard deviation are then reported. The thickness of this deformed layer increases with the sliding cycle number as shown in Figure 8c,d. Figure 8c visualizes that the thickness of this deformed layer depends on crystallographic orientation and is also different at grain boundaries, where it is often larger than inside a grain. For 5000 sliding cycles (Figure 8d), a thickness of the deformed material of $15.73 \pm 1.12\,\mu m$ is measured. Plotting the thickness of the deformed layer against the sliding cycle number in a double logarithmic fashion gives Figure 8e.

These rather qualitative contrast features may give indications on the deformed layer thickness but do not allow to reveal the elementary process governing the change in the subsurface material. Additionally performed cross-sectional EBSD measurements characterize the crystallographic orientation and can be interpreted in terms of geometrically necessary dislocations, similar to the TKD results presented above. Exemplary results after 10, 100, 500, and 5000 reciprocating sliding cycles are presented in **Figure 9**.

In all of these GND density analyses, orientation gradients are observed in the cross-sectional area. These are most pronounced for higher sliding cycle numbers and indicate heavy plastic deformation. This interpretation is further substantiated by the fact that in some cases indexing could not be performed on the entire subsurface area. This indicates high local lattice disturbance. Additionally, an increase in the average GND density is found upon increasing the sliding cycle number from ten to 5000.
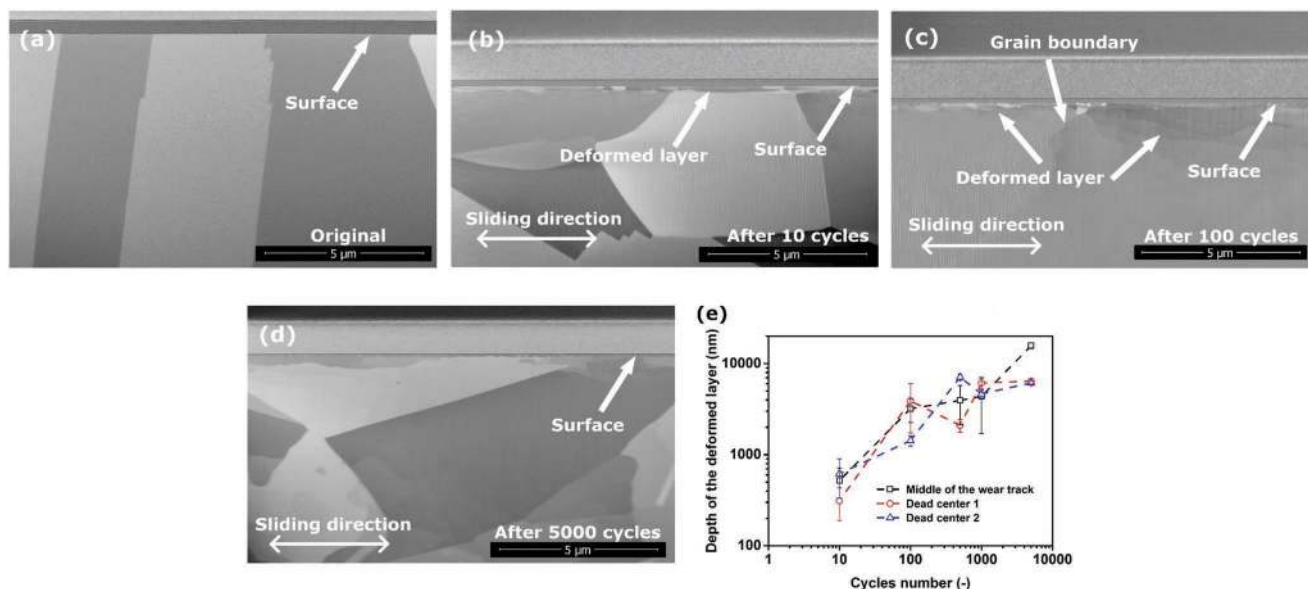

Figure 8. Scanning electron microscopy images after different reciprocating cycle numbers. a) Original material before testing; b) after 10 cycles; c) after 100 cycles; d) after 5000 cycles; e) thickness of the deformed layer, plotted as a function of cycle number. The cross-sections were performed at the middle of the wear track, perpendicular to the sliding surface and parallel to the sliding direction. The contrast at the top of the images is from the two protective platinum layers, the copper surface is marked by arrows. a–e) Reproduced with permission.[66] Copyright 2018, American Chemical Society.
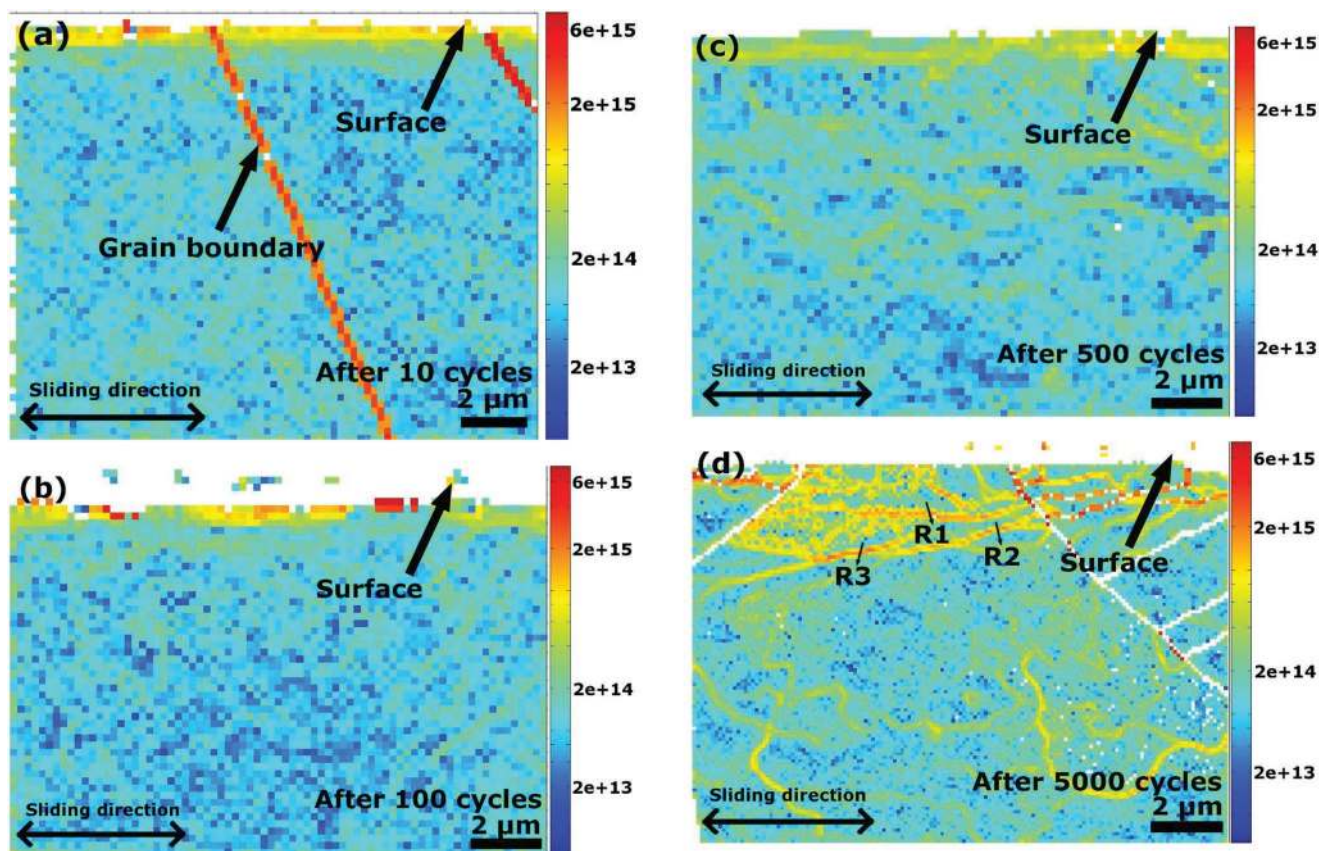
**ADVANCED
SCIENCE NEWS**

www.advancedsciencenews.com

**ADVANCED
MATERIALS**

www.advmat.de

Figure 9. Density of geometrically necessary dislocations in the cross-sectional area of copper wear tracks after different reciprocating cycle numbers: a) after 10 cycles; b) after 100 cycles; c) after 500 cycles; d) after 5000 cycles. The cross-sections were cut perpendicular to the sliding surface and parallel to the sliding direction. The samples' surfaces are marked by black arrows. The color bar in the GND density mapping represents the number of GNDs per unit area (m^2). a–d) Reproduced with permission.[66] Copyright 2018, American Chemical Society.

In all cases, the material closest to the sliding interface has a much higher GND density compared to the material deeper in the bulk of the specimen. This is an agreement with the results presented above and suggests heavy plastic deformation near the sliding surface. In agreement with Figure 8c, in Figure 9a which presents a sample after ten sliding cycles and includes a grain boundary, the GND density is different depending on crystallographic orientation. The grain left of the boundary exhibits a surface normal direction of approximately [001] and shows somewhat higher GND densities reaching deeper than in the right grain that has an orientation close to [101].

In the cross-sectional EBSD results for samples after 100, 500, and 5000 sliding cycles, shown in Figure 9b–d, one observes the initiation of GND density networks, represented as lines of higher dislocation density. This is most pronounced at depth higher than 1 μm and these networks increase in depth and strength as sliding progresses.

When interpreting the contrast changes observed in the images presented in Figure 8, the most likely explanation is that heavy plastic deformation has taken place in the subsurface area. This is also in full agreement with the existing literature.[11,17,32,33] From these images and from plotting the thickness of the deformed layers as a function of the cycle number in Figure 8e, it is obvious that the thickness of the subsurface transformation zone increases with the cycle number,

indicating the amount of plastic deformation is more severe as sliding progresses.

Considering the elastic and plastic anisotropy of copper, it is not surprising that the thickness of the deformed layer depends on the crystallographic orientation. Plastic deformation may be locally more pronounced at and around grain boundaries as these act as dislocation obstacles. This might be the explanation why the thickness of the deformed layer was found to be larger at grain boundaries. Figure 8e can be interpreted as the sensitivity of the material to the structural transformation processes taking place in the subsurface area under the severe conditions imposed by a tribological load. Additionally, the slope in this figure can be thought of as a parameter reflecting the dynamics of the microstructural evolution process. In our case, we found a slope of ≈0.5 in the double logarithmic representation of the data. This corresponds to a thickness growth with the square root of the cycle number. This square root growth interestingly agrees with results that were found by molecular dynamics simulations for the amorphization of diamond in a self-pairing tribological loading scenario.[42] We have now also found very similar growth kinetics for the subsurface transformed zone in Cu–Zn and Cu–Mn alloys as well as in certain steels.[67] This growth law may therefore be of a more general nature.

In combination with the dislocation trace line introduced and discussed in the previous paragraphs, these dislocation

**ADVANCED
SCIENCE NEWS**

www.advancedsciencenews.com

**ADVANCED
MATERIALS**

www.advmat.de

mediated processes can be rationalized as follows: First, dislocations are multiplied in the vicinity of the sliding contact, then they are pushed into the depth of the material and partially pulled back in the wake of the contact where they self-organize into the dislocation trace line. Upon further sliding the density of dislocations increases, leading to the dislocation networks revealed by the cross-sectional EBSD results presented in Figure 9. These processes show a weak orientation dependence. That the grain with a (100) surface orientation exhibits a higher dislocation density compared to the (111) oriented grain is in agreement with both elastic and plastic anisotropy that was found for copper in compression experiments normal to these surfaces. In addition to the GND density networks a rotation of entire grains can be found in the subsurface area for higher cycle numbers. These rotations are for example highlighted by the arrows R1, R2, and R3 in Figure 9d. The rotation angles were 2.5°, 2.7°, and 2.2° around a transverse direction. This is in agreement with previous results and a precursor of the formation of new grain boundaries near the surface. In this premature stage it is apparent that the net grain rotation is induced by dislocation networks and their evolution into subgrain boundaries.

Ultimately, these subgrain boundaries further evolve and result in the refined microstructure shown in Figure 8.

The relatively constant depth of the dislocation trace line may suggest that the trace line does originate from dislocations emitted or multiplied near the contact, while the dislocation processes governing the grain refinement occur deeper in the subsurface area. That different populations of dislocations are responsible for these different phenomena is substantiated by the fact that the dislocation trace line shows only very little dependence on sliding cycle number, while the thickness of the deformed layer exhibits the above-mentioned square-root growth law.

When investigating how a nanocrystalline Ni–W alloy reacts to a tribological load, it was found that also here microstructural changes are confined to a certain area close to the surface.[32] This might be an indication that also in such a case there is a fair amount of dislocation activity very close to the sliding surface. These dislocations near the surface do not, at least not in a decisive way, interact with the maximum Hertzian contact pressure, which is located tens of micrometers underneath the sliding surface. However, dislocations responsible for the microstructural transformations presented in Figure 8, most probably are moved and multiplied, due to these Hertzian stress fields well described by Hamilton theory.[28]

The central role of dislocations for the microstructural transformation processes under the severe conditions imposed by tribological loading have also previously been reported by other researchers.[17,30,68] It should be noted however, that most of the existing literature relies on results from experiments performed with much higher contact stresses and higher wear rates. Wear in our experiments was negligible.

When the shear strain rate was increased to 10^4 s^{-1} and experiments were performed at cryogenic conditions, other deformation mechanisms like twinning were activated.[69] The change from dislocation mediated to twinning mediated plastic deformation will not be further elaborated here.

6. Chemical Aspects

All results presented above are based on a purely mechanistic view of a tribologically loaded surface and are concerned with microstructural aspects of a structural transformation. However, there is also the chemical structure of the sliding surface that needs to be considered. It is well established for example that tribochemical effects can be decisive for the performance of a frictional contact. Therefore, chemical reactions in the context of these mechanical processes can and should not be neglected. Due to the complex composition of almost all technical tribological systems which are made up of the two contacting materials and an optional lubricant, various effects of the different chemical species are possible. The often unknown local temperature rises and high mechanical stresses may lead to tribologically driven chemical reactions that can govern the tribological properties of the entire system.[70] While sliding, the currently prevailing chemical composition as well as the mechanical properties in the contact may therefore significantly vary from those of the materials initially constituting the tribological system. It is for example known that when these intrinsic processes lead to surface layers with higher hardness compared to the initial materials, cracks can be initiated and grown at the interface between these layers and the base material.[71] This increases wear and frictional forces. In case the surface layer is softer compared to the bulk materials, a significant amount of the frictional energy is dissipated in this subsurface layer to grow and plastically deform it.[42] These two examples highlight the need to understand how such chemically different surface layers evolve, while at the same time our knowledge about the pathways for their development is incomplete.

In order to shed some light on tribochemical processes, we again made use of our unlubricated model system consisting of high-purity copper in contact with a sapphire sphere and aimed at elucidating the mechanisms for the formation of surface oxidation during tribological loading. Details of the sample preparation and other experimental procedures can be found in ref [72]. In contrast to the experiments above, the normal load was reduced to 1.5 N, while the tests were again performed in a reciprocating motion and without lubrication, at precisely controlled relative humidity and temperature. The number of reciprocating sliding cycles was systematically increased from 10, 50 to 5000 in order to investigate both the early and late stages of tribologically induced oxidation. The resulting microstructures were investigated by STEM and HRTEM and the chemical composition uncovered by transmission electron microscopy based EDXS.

In **Figure 10**, STEM images taken in high-angle annular dark-field mode (HAADF) for samples after 10, 50 and 5000 sliding cycles are presented. Among the different imaging modes, HAADF is most sensitive to changes in chemical composition, and is often also referred to as Z-contrast. On our specimens, there is no pronounced change in HAADF contrast after ten sliding cycles (Figure 10a) and no other indication for any chemical composition change. This changes after 50 sliding cycles. Figure 10b displays a discontinuous and wavy surface layer with a thickness of roughly 30 nm. The wavy shape observed in this image is the result of semicircular features at the surface that will be referred to as "clusters." That
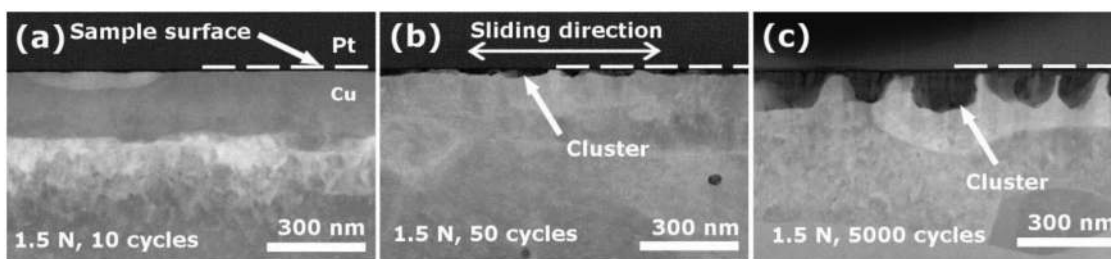
Figure 10. Scanning transmission electron microscopy images of nanocrystalline/amorphous copper oxide clusters at copper surfaces after different reciprocating cycle numbers. Images taken in HAADF mode. a) 10 cycles; b) 50 cycles; c) 5000 cycles. The TEM foils were prepared in the middle of the wear tracks, along the sliding direction perpendicular to the sliding surface. The contrast above the samples' surfaces stems from the protective platinum layer. a–c) Reproduced with permission.[72] Copyright 2018, Elsevier.

the contrast inside this top layer is darker compared to the rest of the cross-section, is a strong indication of a different chemical composition compared to the bulk of the sample. It also suggests that the atomic mass in this layer is smaller compared to copper. When increasing the number of sliding cycles to 5000 (Figure 10c), these clusters have grown in all dimensions. In order to more closely investigate the microstructure inside these clusters, a sample after 50 sliding cycles was investigated via (HR)TEM, shown in **Figure 11**.

The same cluster was observed in bright-field (Figure 11a) and in dark-field conditions (Figure 11b). In the dark-field image, areas with bright contrast are observed inside the cluster. This is an indication that parts of the material constituting these clusters have a similar crystallographic orientation and perhaps even more importantly hints to the existence of some crystallinity within the clusters. This result is supported by the HRTEM image presented in Figure 11c, which is a zoom-in of the same cluster shown in Figure 11a,b, and indicates the existence of nanocrystalline structures in a possibly amorphous matrix.

In order to reveal the quantitative chemical composition of these clusters, TEM-based EDXS was employed. It yielded an oxygen concentration of 7.2% inside the cluster and 2.1% right outside and in the bulk of the material.[72] This suggests that a stoichiometric cuprous oxide (Cu_2O) could not be formed due to an insufficient amount of oxygen available for these tribochemical reactions. It is therefore reasonable to assume that the clusters consist of a mixture of Cu_2O and Cu. Thermodynamic

modeling supports this hypothesis as it found the direct growth of Cu_2O on pure copper surfaces in ambient conditions.[73] Nanobeam diffraction performed inside the TEM and with the same sample as presented in Figure 11 also showed the existence of nanocrystalline Cu_2O.[72] Under the extreme shear imposed by tribological loading, chemical as well as mechanical driving forces apparently act together leading to the formation of these semicircular clusters combining nanocrystalline and amorphous material alike. By comparing EDXS obtained after 50 and 5000 sliding cycles it appears that the clusters simply grow in size but keep their partially nanocrystalline nature. Since we could not find any evidence for such clusters for up to ten sliding cycles, we propose the following sequence for the oxidation of copper under tribological loading: As reported for the native oxidation of copper,[74] the process starts with the formation of amorphous cuprous oxide (Cu_2O) in the form of stochastically distributed and small islands located at the sample surface. The energy barrier for oxidation most likely is lowered at surface steps or other defects or even by the surface roughness, therefore making such locations the most likely candidates for the initiation of oxidation.[75] In the literature and for nontribologically induced oxidation, the growth of individual copper oxide islands has repeatedly been reported.[76] Under the severe mechanical loading conditions imposed by the frictional contact, these oxide islands grow in all three dimensions, still consisting of amorphous Cu_2O and located at and in the sample surface (Figure 10b). Initially the clusters are made up of understoichiometric amorphous Cu_2O. These most probably grow by oxygen
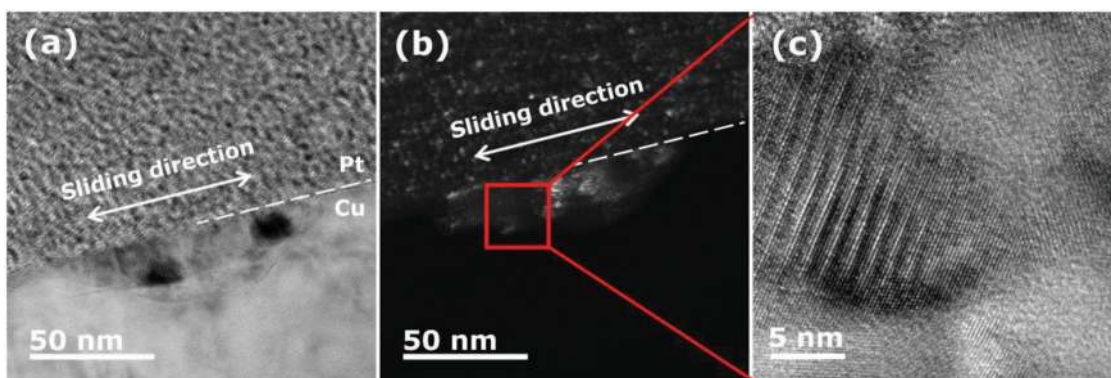

Figure 11. Transmission electron microscopy images of a nanocrystalline / amorphous oxide cluster at a copper surface after 50 reciprocating sliding cycles: a) bright-field image; b) dark-field image from one of the diffraction beams; c) high-resolution image from the area in the red rectangle in (b). The results were taken from the same foil as the one presented in Figure 10b. a–c) Reproduced with permission.[72] Copyright 2018, Elsevier.

1806705 (16 of 19)

**ADVANCED
SCIENCE NEWS**

www.advancedsciencenews.com

**ADVANCED
MATERIALS**

www.advmat.de

entering through the deforming amorphous cluster or through the interface between copper and copper oxide, due to the lack of copper-oxygen surface diffusion.[77] It should be noted however that the exact pathway and the process for forming the nonequilibrium oxygen solution in copper has not been fully revealed; either by us nor in the literature. Since the diffusion of oxygen in pure copper is expected to be considerably smaller compared to interface diffusion, the growth of the copper oxide islands into the clusters of semicircular shape is the consequence and in agreement with our experimental observations.[72]

According to literature, the formation of copper oxide crystals is controlled by the diffusion of oxygen along the boundaries between Cu_2O grains,[78] or at higher temperatures diffusion in Cu_2O.[79] This is an excellent agreement with the hypothesis we stated above and it is quite likely that even though the mechanical driving forces added by a tribological load can be severe, the diffusion pathways are similar compared to static oxidation. Another interesting aspect is whether these oxide clusters grow during the actual passing of the sapphire sphere or in-between the reciprocating loading cycles. Since Cu_2O has a larger specific volume compared to pure copper, one would expect that in case the clusters grew in-between the loading cycles they would protrude the sample surface. When the sapphire sphere then during the next trace were to slide over the newly formed copper oxide, this excess volume would be pushed into the bulk or be smeared over the sample surface. In case the copper oxide islands were to indent the sample, this indentation action would be accompanied by a considerable amount of dislocation activity. No evidence for such dislocation activity was observed experimentally in our electron microscopy investigations. We also did not find any evidence for the copper oxide being smeared over the sample surface. This suggests that the copper oxide clusters are formed while the sphere is actually passing the volume of material in question.

Focusing on the actual friction values, we found that once the sapphire sphere is predominantly sliding on the surface covered by copper oxide clusters, the friction coefficient is reduced to about 0.25 compared to the sphere being in contact with pure copper where a value of 0.35 was measured.[72] This might be due to the fact that the Young's modulus of copper oxide is smaller than that of copper; around 50 MPa compared to 117 GPa respectively.[80]

When sliding progresses, we hypothesize that the amorphous copper oxide clusters keep growing. As this amorphous material is not thermodynamically stable, copper oxide nanocrystals start to nucleate inside the amorphous matrix. We assume this course of events due to the TEM results presented in Figure 11c, where we observed nanocrystalline and amorphous oxides together, while the oxygen-rich layer found after only ten sliding cycles is amorphous.[72] As we had seen in the paragraphs above, for such a small number of sliding cycles grain refinement processes have not yet started, demonstrating that tribologically induced oxidation is a separate and parallel process that has to be investigated separately and that at the same time is of tremendous importance for understanding friction and wear of metallic materials. It needs to be pointed out that besides microstructural and chemical transformations, there are also other dissipation channels in frictional contacts that need to be considered to assess the friction and wear response of materials. Chief among them are the generation of wear particles, frictional heating, sub-surface cracks and phase transformations.[81,82] Discussing all these processes and their consequences in detail is beyond the scope here.

7. Concluding Remarks

Systematic dislocation dynamics modeling in combination with model experiments on high purity copper crystals was able to shed light on the complex and intricate elementary mechanisms governing how materials react to the severe conditions imposed by a tribological load. Herein, we focused our attention on recent results for the structural transformations taking place in the subsurface area of a dry sliding contact. The chemical and microstructural changes taking place in this zone govern the properties of the tribological contact as a whole.

3D discrete dislocation dynamics simulations of a spherical indenter sliding over the smooth surface of a face centered cubic single-crystal demonstrate how dislocations are transported into previously dislocation free regions. The decisive role in this process is played by the stress field of the sliding asperity, as dislocations are trapped under the spherical indenter and tracked along as it continues to slide. This process strongly depends on the orientation of the crystal, the direction of sliding and the Burgers vector of the dislocations. Only dislocations on certain glide planes are selected for transport, depending which of them experience the highest resolved shear stresses. In most cases, glide planes are favored that contain the sliding direction. The absolute length and depth of dislocation transport is a function of the orientation of the glide plane, the sliding direction and the Burgers vectors of the dislocations being transported.

These dislocation transport phenomena, especially in crystals with initially low density of dislocations and under mild loading conditions may be the deciding factor for plastic deformation and changes in surface topography. Even if the contact stresses are too low to nucleate dislocations they may multiply existing ones and transport them into initially dislocation-free areas of the material. From dislocation dynamics simulations it has been possible to develop a criterion for the selection of the glide systems on which dislocations are transported.

For metals, the crucial role of dislocations for their ability to react to the extreme shear imposed by a tribological load is supported by experiments where only one single trace of a sapphire sphere over high-purity copper was performed. Electron microscopy revealed that under the complex stress field of the moving sphere, an organized dislocation structure must have formed at the very beginning of sliding. The horizontal line-like feature that is left after tribological loading and then visible in electron microscopy is called the dislocation trace line. This trace line is found ≈150 nm under the surface and it was consistently observed when performing experiments for a variation of normal loads, sliding passes, crystallographic orientation and different materials. This demonstrates its importance as a precursor for all following microstructural transformations taking place in the subsurface area of a tribologically loaded metal.

Following the structural changes as a function of the sliding cycle number it is found that the thickness of the deformed and structurally altered zone grows into the bulk following a square

1806705 (17 of 19)

root growth law. After 5000 cycles this layer is ≈10 μm thick. Already after a few hundred sliding cycles a network of geometrically necessary dislocations has started to self-organize into distinct wall-like structures which appears to be the elementary mechanism for the formation of sub-grains and the following grain refinement.

Yet another process is the sliding induced oxidation that takes place at the sliding contact in parallel to the dislocation dominated subsurface structural transformations. Especially for higher sliding numbers the tribological performance of the contact will be crucially determined by this oxide layer covering the surface. We revealed that sliding induced oxidation starts with the formation of randomly distributed amorphous copper oxide (Cu_2O) patches at the sample surface. These grow into amorphous oxide islands and further form semicircular amorphous clusters. Once a critical size of these clusters has been reached and due to the inherent thermodynamic instability of the amorphous material inside, Cu_2O nanocrystals nucleate and grow. These processes most probably are due to a combination of mechanical and chemical driving forces.

The fundamental understanding of all of these elementary mechanisms taking place under the high shear conditions imposed on metals subjected to a tribological load is necessary for the future modeling of a material's response to a sliding contact. The research summarized here is a first step toward the goal of guiding the design of alloys and the processing of materials with superior friction and wear properties even if achieving it might be years away.

Supporting Information

Supporting Information is available from the Wiley Online Library or from the authors.

Acknowledgements

Conflict of Interest

The authors declare no conflict of interest.

Keywords

[1] J. G. J. Olivier, G. Janses-Maenhout, *CO2 Emissions from Fossil Fuel Combustion Part III: Total Green House Gas Emissions*, International Energy Agency, **2015**; *NOAA National Centers for Environmental Information*.

[2] K. Holmberg, P. Andersson, A. Erdemir, *Tribol. Int.* **2012**, *47*, 221.

[3] O. Pinkus, D. F. Wilcock, *Strategy for Energy Conservation through Tribology*, American Society of Mechanical Engineers, New York **1977**.

[4] H. P. Jost, *Wear* **1990**, *136*, 1.

[5] B. Bhushan, *Introduction to Tribology*, John Wiley & Sons, Inc., New York **2002**.

[6] L. Da Vinci, *Notebooks of Leonardo Da Vinci*, David Laine, New York **1939**.

[7] G. Binnig, C. F. Quate, C. Gerber, *Phys. Rev. Lett.* **1986**, *56*, 930.

[8] C. M. Mate, G. M. McClelland, R. Erlandsson, S. Chiang, *Phys. Rev. Lett.* **1987**, *59*, 1942.

[9] M. Urbakh, E. Meyer, *Nat. Mater.* **2010**, *9*, 8.

[10] S. Li, Q. Li, R. W. Carpick, P. Gumbsch, X. Z. Liu, X. Ding, J. Sun, J. Li, *Nature* **2016**, *539*, 541.

[11] D. A. Rigney, W. A. Glaeser, *Wear* **1978**, *46*, 241.

[12] a) D. A. Rigney, J. P. Hirth, *Wear* **1979**, *53*, 345; b) K. H. Zum Gahr, *Wear* **1981**, *74*, 353.

[13] P. J. Blau, *Tribol. Int.* **2005**, *38*, 1007.

[14] A. Brink, K. Lichtenberg, M. Scherge, *Wear* **2016**, *360–361*, 114.

[15] F. P. Bowden, D. Tabor, *The Friction and Lubrication of Solids*, Clarendon Press, Oxford, UK **1950**.

[16] a) T. Hattori, Y. Kaneko, S. Hashimoto, *J. Mater. Sci.* **2008**, *43*, 3923; b) P. Stoyanov, P. A. Romero, R. Merz, M. Kopnarski, M. Stricker, P. Stemmer, M. Dienwiebel, M. Moseler, *Acta Mater.* **2014**, *67*, 395.

[17] D. Hughes, N. Hansen, *Phys. Rev. Lett.* **2001**, *87*, 135503.

[18] a) D. A. Hughes, N. Hansen, *Phys. Rev. Lett.* **2001**, *87*, 135503; b) S. Karthikeyan, H. J. Kim, D. A. Rigney, *Phys. Rev. Lett.* **2005**, *95*, 106001; c) K. Lu, *Science* **2014**, *345*, 1455.

[19] a) F. P. Bowden, D. Tabor, *The Friction and Lubrication of Solids*, Clarendon Press, Oxford, UK **1986**; b) D. Rigney, S. Karthikeyan, *Tribol. Lett.* **2010**, *39*, 3.

[20] a) N. K. Sundaram, Y. Guo, S. Chandrasekar, *Phys. Rev. Lett.* **2012**, *109*, 106001; b) A. Mahato, Y. Guo, N. K. Sundaram, S. Chandrasekar, *Proc. R. Soc. A* **2014**, *470*, 20140297.

[21] N. Beckmann, P. A. Romero, D. Linsler, M. Dienwiebel, U. Stolz, M. Moseler, P. Gumbsch, *Phys. Rev. Appl.* **2014**, *2*, 064004.

[22] X. Chen, Z. Han, X. Li, K. Lu, *Sci. Adv.* **2016**, *2*, e1601942.

[23] a) J. B. Singh, J. G. Wen, P. Bellon, *Acta Mater.* **2008**, *56*, 3053; b) X. Chen, Z. Han, K. Lu, *Wear* **2014**, *320*, 41.

[24] P. Stemmer, A. Fischer, *Lubricants* **2018**, *6*, 34.

[25] D. A. Rigney, S. Karthikeyan, *Tribol. Lett.* **2010**, *39*, 3.

[26] N. Argibay, T. Furnish, B. Boyce, B. Clark, M. Chandross, *Scr. Mater.* **2016**, *123*, 26.

[27] N. Argibay, M. Chandross, S. Cheng, J. R. Michael, *J. Mater. Sci.* **2017**, *52*, 2780.

[28] G. M. Hamilton, *Proc. Inst. Mech. Eng., Part C* **1983**, *197*, 53.

[29] a) A. Emge, S. Karthikeyan, H. J. Kim, D. A. Rigney, *Wear* **2007**, *263*, 614; b) P. Heilmann, W. A. T. Clark, D. A. Rigney, *Acta Metall.* **1983**, *31*, 1293.

[30] a) D. Turley, L. Samuels, *Metallography* **1981**, *14*, 275; b) D. Hughes, D. Dawson, J. Korellis, L. Weingarten, *Wear* **1995**, *181–183*, 458.

[31] S. Korres, T. Feser, M. Dienwiebel, *Acta Mater.* **2012**, *60*, 420.

[32] T. J. Rupert, C. A. Schuh, *Acta Mater.* **2010**, *58*, 4137.

[33] W. L. Li, N. R. Tao, Z. Han, K. Lu, *Wear* **2012**, *274–275*, 306.

[34] Z.-P. Luo, G.-P. Zhang, R. Schwaiger, *Scr. Mater.* **2015**, *107*, 67.

[35] J. F. Curry, T. F. Babuska, T. A. Furnish, P. Lu, D. P. Adams, A. B. Kustas, B. L. Nation, M. T. Dugger, M. Chandross, B. G. Clark, B. L. Boyce, C. A. Schuh, N. Argibay, *Adv. Mater.* **2018**, *30*, 1802026.

[36] a) A. Emge, S. Karthikeyan, D. A. Rigney, *Wear* **2009**, *267*, 562; b) M. S. Bednar, D. Kuhlmann-Wilsdorf, *Wear* **1995**, *181–183*, 922;

**ADVANCED
SCIENCE NEWS**

www.advancedsciencenews.com

**ADVANCED
MATERIALS**

www.advmat.de

c) D. Shakhvorostov, L. Jian, E. Nold, G. Beuchle, M. Scherge, *Tribol. Lett.* **2007**, *28*, 307.

[37] K. L. Hsu, T. M. Ahn, D. A. Rigney, *Wear* **1980**, *60*, 13.

[38] R. Pourzal, R. Theissmann, B. Gleising, S. Williams, A. Fischer, *Mater. Sci. Forum* **2010**, *638–642*, 1872.

[39] P. A. Romero, T. T. Jarvi, N. Beckmann, M. Mrovec, M. Moseler, *Phys. Rev. Lett.* **2014**, *113*, 5.

[40] J. E. Hammerberg, B. L. Holian, T. C. Germann, R. Ravelo, *Metall. Mater. Trans. A* **2004**, *35*, 2741.

[41] S. Karthikeyan, A. Agrawal, D. A. Rigney, *Wear* **2009**, *267*, 1166.

[42] L. Pastewka, S. Moser, P. Gumbsch, M. Moseler, *Nat. Mater.* **2011**, *10*, 34.

[43] J. L. Young, D. Kuhlmann-Wilsdorf, R. Hull, *Wear* **2000**, *246*, 74.

[44] D. A. Hughes, N. Hansen, *Phys. Rev. Lett.* **2014**, *112*.

[45] J. Gagel, D. Weygand, P. Gumbsch, *Acta Mater.* **2016**, *111*, 399.

[46] a) C. L. Kelchner, S. J. Plimpton, J. C. Hamilton, *Phys. Rev. B* **1998**, *58*, 11085; b) W. W. Gerberich, J. C. Nelson, E. T. Lilleodden, P. Anderson, J. T. Wyrobek, *Acta Mater.* **1996**, *44*, 3585.

[47] a) S. Y. Tarasov, A. V. Chumaevskii, D. V. Lychagin, A. Y. Nikonov, A. I. Dmitriev, *Wear* **2018**, *410–411*, 210; b) D. Buckley, R. Johnson, *Wear* **1968**, *11*, 405.

[48] V. Deshpande, D. Balint, A. Needleman, E. Van der Giessen, *Modell. Simul. Mater. Sci. Eng.* **2007**, *15*, S97.

[49] F. Sun, E. van der Giessen, L. Nicola, *Acta Mater.* **2016**, *109*, 162.

[50] a) R. Komanduri, N. Chandrasekaran, L. Raff, *Wear* **2000**, *240*, 113; b) K. Sun, L. Fang, Z. Yan, J. Sun, *Wear* **2013**, *303*, 191; c) J. Li, Q. Fang, Y. Liu, L. Zhang, *Int. J. Adv. Manuf. Technol.* **2015**, *77*, 1057.

[51] S. Jun, Y. Lee, S. Y. Kim, S. Im, *Nanotechnology* **2004**, *15*, 1169.

[52] a) Y. Tsuya, *Wear* **1969**, *14*, 309; b) J. Ko, A. Gellman, *Langmuir* **2000**, *16*, 8343.

[53] C. M. Mancinelli, A. J. Gellman, *Langmuir* **2004**, *20*, 1680.

[54] a) D. Weygand, L. H. Friedman, E. van der Giessen, A. Needleman, *Mater. Sci. Eng., A* **2001**, *309–310*, 420; b) D. Weygand, P. Gumbsch, *Mater. Sci. Eng., A* **2005**, *400–401*, 158; c) D. Weygand, J. Senger, C. Motz, W. Augustin, V. Heuveline, P. Gumbsch, in *High Performance Computing in Science and Engineering '08*, (Eds.: W. E. Nagel, D. B. Kroner, M. M. Resch), Springer Verlag Berlin, **2009**, pp. 507–523.

[55] D. Weygand, L. H. Friedman, E. V. d. Giessen, A. Needleman, *Modell. Simul. Mater. Sci. Eng.* **2002**, *10*, 437.

[56] J. Gagel, D. Weygand, P. Gumbsch, *Acta Mater.* **2018**, *156*, 215.

[57] E. Van der Giessen, A. Needleman, *Modell. Simul. Mater. Sci. Eng.* **1995**, *3*, 689.

[58] a) E. Bitzek, P. Gumbsch, *Mater. Sci. Eng., A* **2004**, *387–389*, 11; b) E. Bitzek, D. Weygand, P. Gumbsch, presented at IUTAM Symposium on Mesoscopic Dynamics of Fracture Process and Materials Strength, Dordrecht, The Netherlands, September **2004**.

[59] Ø. Ryen, B. Holmedal, O. Nijs, E. Nes, E. Sjölander, H.-E. Ekström, *Metall. Mater. Trans. A* **2006**, *37*, 1999.

[60] S. Brinckmann, G. Dehm, *Wear* **2015**, *338–339*, 436.

[61] C. Greiner, Z. Liu, R. Schneider, L. Pastewka, P. Gumbsch, *Scr. Mater.* **2018**, *153*, 63.

[62] a) D. Santhiya, Z. Burghard, C. Greiner, L. P. Jeurgens, T. Subkowski, J. Bill, *Langmuir* **2010**, *26*, 6494; b) P. W. Trimby, Y. Cao, Z. Chen, S. Han, K. J. Hemker, J. Lian, X. Liao, P. Rottmann, S. Samudrala, J. Sun, *Acta Mater.* **2014**, *62*, 69.

[63] a) H. Gao, Y. Huang, W. D. Nix, J. W. Hutchinson, *J. Mech. Phys. Solids* **1999**, *47*, 1239; b) M. Calcagnotto, D. Ponge, E. Demir, D. Raabe, *Mater. Sci. Eng., A* **2010**, *527*, 2738.

[64] D. Hull, D. J. Bacon, *Introduction to Dislocations*, Butterworth-Heinemann, Oxford, UK **2011**.

[65] J. P. J. , Z. S. Basinski, *Can. J. Phys.* **1967**, *45*, 707.

[66] C. Greiner, Z. Liu, L. Strassberger, P. Gumbsch, *ACS Appl. Mater. Interfaces* **2016**, *8*, 15809.

[67] C. Greiner, Z. Liu, P. Messer, S. Laube, unpublished.

[68] D. A. Hughes, N. Hansen, *Philos. Mag.* **2003**, *83*, 3871.

[69] X. Chen, R. Schneider, P. Gumbsch, C. Greiner, *Acta Mater.* **2018**.

[70] W. Tysoe, *Tribol. Lett.* **2017**, *65*, 48.

[71] Z. N. Farhat, Y. Ding, D. O. Northwood, A. T. Alpas, *Mater. Sci. Eng., A* **1996**, *206*, 302.

[72] Z. Liu, C. Patzig, S. Selle, T. Höche, P. Gumbsch, C. Greiner, *Scr. Mater.* **2018**, *153*, 114.

[73] F. Reichel, L. Jeurgens, E. Mittemeijer, *Thin Solid Films* **2008**, *516*, 1457.

[74] A. Soon, M. Todorova, B. Delley, C. Stampfl, *Phys. Rev. B* **2007**, *75*, 125420.

[75] C. P. León, C. Sürgers, H. v. Löhneysen, *Phys. Rev. B* **2012**, *85*, 035434.

[76] a) G. W. Zhou, *Acta Mater.* **2009**, *57*, 4432; b) J. H. Ho, R. W. Vook, *J. Cryst. Growth* **1978**, *44*, 561.

[77] J. C. Yang, B. Kolasa, J. M. Gibson, M. Yeadon, *Appl. Phys. Lett.* **1998**, *73*, 2841.

[78] S.-K. Lee, H.-C. Hsu, W.-H. Tuan, *Mater. Res.* **2016**, *19*, 51.

[79] T. Suzuki, *J. Phys. Soc. Jpn.* **1960**, *15*, 2018.

[80] M. H. Manghnani, W. S. Brower, H. S. Parker, *Phys. Status Solidi A* **1974**, *25*, 69.

[81] a) W. G. Sawyer, N. Argibay, D. L. Burris, B. A. Krick, *Annu. Rev. Mater. Res.* **2014**, *44*, 395; b) D. Shakhvorostov, K. Pohlmann, M. Scherge, *Wear* **2004**, *257*, 124.

[82] C. Greiner, M. Schafer, U. Popp, P. Gumbsch, *ACS Appl. Mater. Interfaces* **2014**, *6*, 7986.